Contrib Mineral Petrol (2012) 163:725–743
DOI 10.1007/s00410-011-0696-2

ORIGINAL PAPER

Crustal homogenization revealed by U–Pb zircon ages and Hf isotope evidence from the Late Cretaceous granitoids of the Agaçören intrusive suite (Central Anatolia/Turkey)

Serhat Köksal · Andreas Möller · M. Cemal Göncüoglu · Dirk Frei · Axel Gerdes

Received: 17 October 2009 / Accepted: 14 September 2011 / Published online: 4 October 2011

Abstract Geochemical and isotopic evidence from the Agaçören Igneous Association in central Anatolia-Turkey indicates that this suite of calc-alkaline granitic rocks have undergone crustal homogenization during regional metamorphic and related magmatic events. Whole-rock chemical and Sr–Nd isotopic data of the granitoids reveal crustal affinity with an earlier subduction component. Zircons show inherited cores and subsequent magmatic overgrowths. The laser ablation ICP-MS $^{206}Pb/^{238}U$ zircon ages are determined as 84.1 ± 1.0 Ma for the biotite-muscovite granite, 82.3 + 0.8/−1.1 Ma for the hornblende-biotite granite, 79.1 + 2.1/−1.5 Ma for the granite porphyry dyke, 75.0 + 1.0/−1.0 Ma for the alkali feldspar dyke, and 73.6 ± 0.4 Ma for the monzonite. This is interpreted as continuous magma generation, possibly from heterogeneous sources, from ca. 84 to 74 Ma during the closure of the northern branch of the Neotethyan Ocean. The oldest granitoids (84–82 Ma) were probably formed due to crustal thickening after obduction of the MORB-type oceanic crust onto the Tauride-Anatolide microplate. The younger granitoids are interpreted to be related to the subsequent post-collisional extension after lithospheric delamination. Combination of the laser ablation ICP-MS zircon Lu–Hf isotope data with the U–Pb ages of inherited cores suggests that Cretaceous granitoids formed by melting of heterogeneous crustal protoliths, which results in significant variation in $\varepsilon Hf_{(t)}$ data (from −12.9 to +2.2). These protoliths were probably composed of reworked Early Proterozoic crust, minor juvenile Late Proterozoic magmatic components, and Paleozoic to pre-Late Cretaceous recycled crustal material. Moreover, the Late Cretaceous zircon domains of the different granitoids are characterized by a crustal signature, with a relatively restricted zircon $\varepsilon Hf_{(t)}$ data ranging from −4.1 to −8.8. This variation is only about twice the reproducibility (ca. ±1 εHf) of the data, but

Communicated by J. Hoefs.

Electronic supplementary material The online version of this article (doi:10.1007/s00410-011-0696-2) contains supplementary material, which is available to authorized users.

S. Köksal (✉)
Central Laboratory, R&D Research and Training Center, Radiogenic Isotope Laboratory, Middle East Technical University, 06531 Ankara, Turkey
e-mail: skoksal@metu.edu.tr

A. Möller
Department of Geology, University of Kansas, 1475 Jayhawk Boulevard, 120 Lindley Hall, Lawrence, KS 66045-7613, USA
e-mail: amoller@ku.edu

M. C. Göncüoglu
Department of Geological Engineering, Middle East Technical University, 06531 Ankara, Turkey
e-mail: mcgoncu@metu.edu.tr

D. Frei
Department of Earth Sciences, Stellenbosch University, Private Bag X1, Matieland 7602, South Africa
e-mail: frei@sun.ac.za

A. Gerdes
Institut für Geowissenschaften, Johann Wolfgang Goethe University, Altenhoeferallee 1, 60438 Frankfurt Am Main, Germany
e-mail: gerdes@em.uni-frankfurt.de

much smaller than the isotope variability of inherited zircons. Our preferred interpretation is effective isotopic homogenization of the heterogeneous central Anatolian crust during the Late Cretaceous high-grade metamorphic and magmatic events, a process that we propose to be relevant for other active continental margins.

Keywords Zircon · Agaçören · Turkey · Crustal homogenization · Lu–Hf isotopes · Laser ablation ICP-MS · Geochronology

Introduction

Zircon is a key mineral for determining petrogenetic processes in the geological history of crustal and mantle systems because of its substantial chemical and physical stability (e.g., Hanchar and Miller 1993; Harley and Kelly 2007). In situ microanalytical techniques can be used to obtain ages, as well as elemental and isotopic fingerprints from zircon and help to link this with the petrogenetic history of the host rocks (e.g., Hoskin et al. 2000; Belousova et al. 2002; Hawkesworth and Kemp 2006a; Kemp et al. 2006; Scherer et al. 2007; Harley and Kelly 2007). Among the in situ dating methods, U–Pb dating of zircon by laser ablation (LA) ICP-MS has been demonstrated to be capable of producing data with similar precision to those of ion probe analyses (e.g., Košler et al. 2002; Jackson et al. 2004; Gerdes and Zeh 2006; Frei and Gerdes 2009). Additionally, Lu–Hf isotope measurements by laser ablation ICP-MS on zircon crystals reveal significant information on the magma genesis and crustal evolution (e.g., Hawkesworth and Kemp 2006a, b; Yang et al. 2006). Combining Lu–Hf isotope data with the U–Pb crystallization ages of the zircons is very useful in resolving the relationship between the major episodes of igneous activity and formation of new crust (e.g., Hawkesworth and Kemp 2006a).

Determination of the petrogenetic history and crystallization age of a granitoid supplies particularly important data if the granitoid presents a time-marker in the tectonic history of an orogenic belt (e.g., Harris 1996). The intrusion of granitoids in central Anatolia can be directly related to the closure of the Tethys Ocean (Göncüoglu et al. 1997, 2007), and these magmatic bodies thus provide key information on the geotectonic evolution of Anatolia and its surrounding area. Existing geochronological data have shown that these granitoids are Late Cretaceous (e.g., Ataman 1972; Göncüoglu 1986; Kadioglu et al. 2003; Köksal et al. 2004, 2007; Ilbeyli et al. 2004; Boztug et al. 2007a, b, c). Petrogenesis of the central Anatolian granitoids (CAG) has been the subject of numerous geochemical and geochronological studies that have resulted in different models for their evolution (e.g., Göncüoglu and Türeli 1994; Boztug 1998, 2000; Düzgören-Aydin et al. 2001; Ilbeyli et al. 2004; Ilbeyli 2005; Kadioglu et al. 2003, 2006; Boztug et al. 2007a, b, c), ranging from arc to collisional/post-collisional magmatism. The results also disagree on timing of the granitoid intrusions. A better understanding of the magmatic processes therefore has to be achieved to unravel the geodynamic events during Alpine closure of the Izmir-Ankara-Erzincan Ocean, the main oceanic branch of the Neotethys in the eastern Mediterranean. To test the geological and petrogenetic constraints of previous studies and to improve existing models for the CAG, we carried out new isotope measurements on zircons to address the exact timing of crystallization and the involvement of inherited crustal components.

The Agaçören Igneous Association (AIA) is one of the largest intrusive suites in central Anatolia. Our research focuses on detailed U–Pb geochronological, Lu–Hf isotopic and typological studies of zircon crystals in the AIA granitoids, to study granitoid generation and crust formation in this segment of the Tethyan region.

Geological framework

Turkey is the geological centerpiece for the geodynamic evolution of the Alpine Tethys (Neotethys). The Izmir-Ankara-Erzincan Ocean is one of the branches of the Neotethys, with the Tauride-Anatolide continental microplate in the south and the Rhodope-Pontide continental microplate in the north (for a brief review see e.g., Sengör and Yilmaz 1981). Before juxtaposition of the Tauride-Anatolide microplate and the Pontides along the Izmir-Ankara-Erzincan suture zone (IAESZ) in Late Cretaceous times, both plates underwent rather different geological histories. The Tauride-Anatolide microplate was initially separated from Gondwana by the opening of the Southern Branch of Neotethys in the Late Permian-Early Mesozoic (e.g., Göncüoglu et al. 1997, 2007; Stampfli and Borel 2002). The Central Anatolian Crystalline Complex (CACC) forms the northern, telescoped margin of Tauride-Anatolide microplate during the Alpine closure of the Neotethys (e.g., Göncüoglu 2010). The Sakarya continent, a composite terrane with pre-Jurassic basement, was bounded by the Intra-Pontide Suture in the north and the Izmir-Ankara-Erzincan Ocean to the south and formed the main northern segment of the Alpine collision (e.g., Göncüoglu et al. 1997).

The main rock suites of the CACC are the metamorphic basement rocks of Precambrian–Palaeozoic–Mesozoic age, supra-subduction zone type ophiolitic units derived from the IAESZ and overthrust onto the metamorphic rocks, and the CAG intruding both the metamorphic and ophiolitic rocks (e.g., Göncüoglu et al. 1997; Yaliniz et al. 1999)

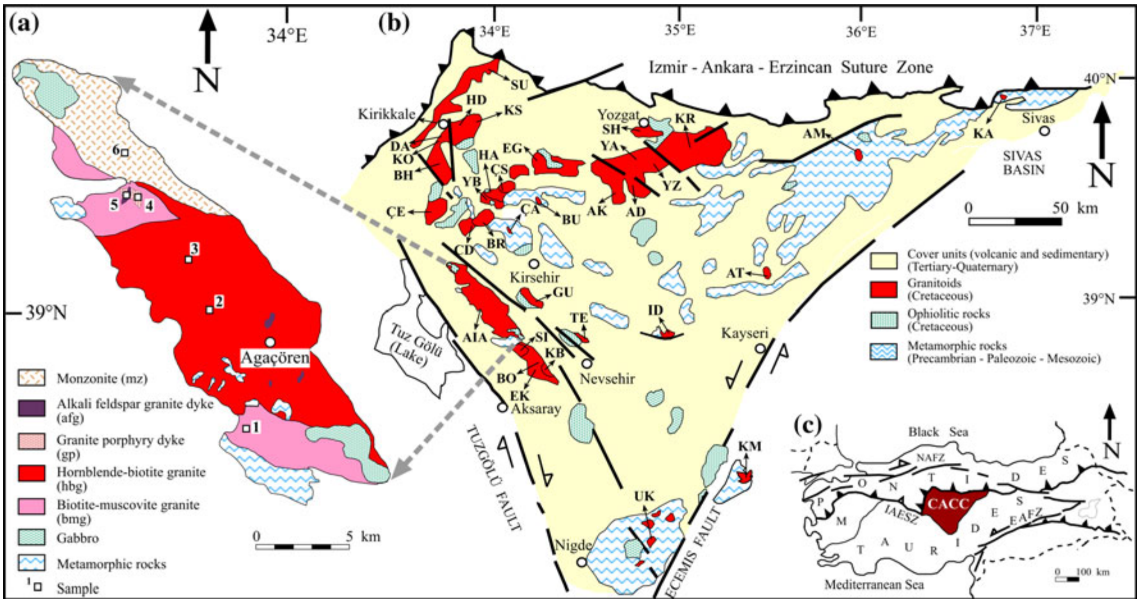

Fig. 1 **a** Geological map of the study area (after Kadioglu 1996; Kadioglu et al. 2003, 2006), **b** Simplified geological map of the Central Anatolian Crystalline Complex (after Bingöl 1989; Göncüoglu and Türeli 1994; Boztug 2000; Düzgören-Aydin et al. 2001; Toksoy-Köksal et al. 2001). *Central Anatolian granitoids*: AD—Adatepe, AIA—Agaçören igneous association, AK—Akçakoyunlu, AM—Akdagmadeni, AT—Atdere, BE—Behrekdag igneous association, BO—Borucu, BR—Baranadag, BU—Buzlukdag, ÇA—Çayagzi, CD—Cefalikdag, ÇE—Çelebi, ÇS—Çamsari, DA—Danaciobasi, EG—Egrialan, EK—Ekecikdag igneous association, GU—Gümüskent, HA—Hamit, HD—Hasandede, ID—Idisdag, KA—Karaçayir, KB—Kalebalta, KM—Karamadazi, KO—Konur, KR—Kerkenez, KS—Keskin, SH—Sarihacili, SI—Sinandı, SU—Sulakyurt, TE—Terlemez, UK—Uçkapılı, YA—Yassiagil, YB—Bayindir, YZ—Yozgat igneous association. **c** Inset map showing the main tectonic units in Turkey. *CACC* Central Anatolian Crystalline Complex; *M* Menderes Massif; *IAESZ* Izmir-Ankara-Erzincan suture zone; *NAFZ* North Anatolian Fault zone; *EAFZ* East Anatolian Fault zone

(Fig. 1). Younger, overlying non-metamorphic units are Late Maastrichtian clastic rocks, Paleocene–Eocene volcanic, volcanoclastic and sedimentary rocks, and Neogene-Quaternary Cappadocian volcanic rocks, carbonate and clastic cover units (e.g., Aydar et al. 1995; Göncüoglu et al. 1997; Köksal et al. 2001) (Fig. 1).

Granitoids in the Agaçören area intrude the metamorphic basement that mainly consists of marbles and have sinusoidal and irregular contacts with gabbro units, with compositional changes along these contacts (Kadioglu and Güleç 1996). These contact relationships together with their identical Ar–Ar ages lead to the interpretation of coeval formation of granitoids and gabbros within the AIA (Kadioglu et al. 2003). Other authors, however, (e.g., Göncüoglu et al. 1991; Göncüoglu and Türeli 1994; Yaliniz et al. 1996, 1999; Yilmaz and Boztug 1998; Floyd et al. 1998, 2000; Toksoy-Köksal et al. 2001; Koçak et al. 2005; Ilbeyli 2008) described the gabbros within the central Anatolia as remnants of the ophiolitic units and as roof pendants on the granitic rocks, which we accept as the most likely model.

The granitoids within the AIA are subdivided into the biotite-muscovite granite (bmg), the hornblende-biotite granite (hbg), the granite porphyry dyke (gp), the alkali feldspar granite dyke (afg), and the monzonite (mz) based on their mineralogical and petrographic characteristics, as proposed by previous authors (e.g., Kadioglu 1996; Kadioglu and Güleç 1996; Güleç and Kadioglu 1998; Kadioglu et al. 2003, 2006; Köksal et al. 2007) (Fig. 1). The hornblende-biotite granite intruded the biotite-muscovite granite, whereas the monzonite intruded both (e.g., Kadioglu et al. 2006) (Fig. 1). Dykes of granite porphyry cut the biotite-muscovite and hornblende-biotite granites, while the alkali feldspar granite intrudes into the biotite-muscovite granite, the hornblende-biotite granite and the granite porphyry (e.g., Kadioglu et al. 2006), which firmly establishes the relative age sequence for the intrusive events (Fig. 1).

Analytical methods

Zircon crystals were concentrated by standard separation techniques (i.e., crushing, grinding, sieving, heavy mineral enrichment by Wilfley table, heavy liquids and magnetic separation), and were handpicked under a binocular microscope. Unbroken and euhedral zircon crystals representing all zircon populations in the samples were separated for zircon typological investigation and scanning electron microscope (SEM), cathodoluminescence (CL), and laser ablation ICP-MS studies. SEM and CL studies were carried out at the GeoForschungsZentrum (GFZ)-Potsdam with a DSM 962/Zeiss scanning electron microscope equipped with a polychromatic Zeiss CL detector, using a 15 kV accelerating potential. Overviews and morphology images of the gold–palladium coated complete zircons mounted on sticky tape were taken with the SE (secondary electron)-detector. The same grains were then embedded in epoxy and polished down to approximately half their thickness and carbon-coated for the CL-study.

Another group of the handpicked grains were mounted in epoxy, sectioned to about half their thickness, and polished for the laser ablation-sector field (LA-SF)-ICP-MS measurements. Back-scattered electron (BSE) images were taken using a Philips XL 40 SEM at Geological Survey of Denmark and Greenland (GEUS) to evaluate zircon textures and select domains to be analyzed. Prior to U–Pb dating, the carbon coating necessary for BSE imaging was removed, and the mounts were subsequently cleaned in different steps with ethanol and de-ionized water in an ultrasonic bath to remove surface lead contamination before introduction into the sample cell; thus, no pre-ablation was done for removal of surface contamination. The initial parts of the signals have been discarded in some rare cases if a surface lead contamination was detected during analysis.

In situ LA-SF-ICP-MS U–Pb zircon measurements were performed on a Thermo Scientific Element2 high resolution magnetic sector field ICP-MS coupled with a Merchantek New Wave 213 nm UV laser ablation system at GEUS. The methods applied essentially followed those described in detail by Frei and Gerdes (2009) and Gerdes and Zeh (2006). Laser spot sizes of 30 or 40 µm were used for laser ablation, depending on the size and complexity of the analyzed zircons. The GJ1 zircon was used as a primary reference standard (e.g., Jackson et al. 2004) to correct for instrumental mass-bias. For quality control purposes, the Plešovice (Sláma et al. 2008) and M127 (Nasdala et al. 2008) zircon standard materials are analyzed as secondary standards within each analytical session at the GEUS LA-SF-ICP-MS laboratory. The age results obtained for both zircons are consistent, within the 2 sigma error limits, with the ID-TIMS values reported by Sláma et al. (2008) and Nasdala et al. (2008).

Lutetium–Hafnium isotopes were analyzed using a Thermo Scientific Neptune multi-collector ICP-MS at Goethe-University Frankfurt coupled with the same model of laser and ablation cell as at GEUS, on selected previously dated zircon grains, using the methods described in Gerdes and Zeh (2006, 2009). Data were collected in static mode during 60s of ablation with a spot size of 40 µm. Eleven laser ablation multi-collector (LA-MC)-ICP-MS analyses of the GJ-1 zircon (ca. 9,600 ppm Hf) during our analytical session gave a $^{176}Hf/^{177}Hf$ ratio of 0.282005 ± 13 (2 sigma), which is within error identical to results obtained by solution MC-ICP-MS analyses of the Lu and Yb free Hf fraction (0.281998 ± 7, 2 sigma; Gerdes, unpublished data). In order to show that the analyzed zircon zones are homogenous with respect to the Lu–Hf system, double-measurements were obtained on one grain (Table 2, Online Resource 2). Uncertainties given for the Lu–Hf analyses are at the 2-sigma level.

Whole-rock elemental geochemical analyses were performed at ACME Analytical Laboratories Ltd. (Canada) using their standard analytical procedures. Major elements were determined by ICP-AES after fusion with $LiBO_2$/$Li_2B_4O_7$. Trace and rare-earth elements were determined by ICP-MS after acid decomposition (5% HNO_3). Major element concentrations are well above the detection limits. Trace elements and REE detection limits are: 8 ppm for V, 1 ppm for Ba and Sn, 0.5 ppm for Sr and W, 0.3 ppm for Nd, 0.2 ppm for Co and Th, 0.1 ppm for Cs, Hf, Nb, Rb, Ta, U, Y, Zr, La and Ce, 0.05 ppm for Sm, Gd, Dy, Yb, 0.03 ppm for Er, 0.02 ppm for Pr, Eu and Ho, and 0.01 for Tb, Tm, Lu.

Strontium and Nd isotopic whole-rock analyses were performed at the Radiogenic Isotope Laboratory of Middle East Technical University Central Laboratory, using the analytical methods described in detail by Köksal and Göncüoglu (2008). Powdered rock samples were dissolved with 4 ml of 52% HF for 4 days at 160°C on a hot plate, then dried and dissolved overnight in 4 ml 6 N HCl at 160°C on a hot plate. Strontium was separated in 2.5 N HCl with 2 ml Bio Rad AG50 W-X12, 100–200 mesh resin. The REE fraction was collected from Sr cation exchange columns with 6 N HCl after Sr was separated. Neodymium was separated from the REE fraction in 0.022 N HCl with 2 ml biobeads (Bio Rad) coated with HDEHP (bis-2-ethylhexyl phosphoric acid). Strontium was loaded on single Re-filaments with a Ta-activator and 0.005 N H_3PO_4, and Nd was loaded on double Re-filaments with 0.005 N H_3PO_4. Strontium and Nd isotopic compositions were determined on a Thermo Scientific Triton TI Multi-Collector Thermal Ionization mass spectrometer using static multi-collection. Analytical uncertainties are given at 2-sigma$_m$ level. Ratios of $^{87}Sr/^{86}Sr$ are normalized to $^{86}Sr/^{88}Sr = 0.1194$, and $^{143}Nd/^{144}Nd$ data are normalized to $^{146}Nd/^{144}Nd = 0.7219$. During the course of the measurement, NBS 987 and Nd LaJolla were measured as 0.710244 ± 8 ($n = 3$) and 0.511852 ± 2 ($n = 2$), respectively. The USGS reference material BCR-1 gave $^{87}Sr/^{86}Sr = 0.705014 \pm 5$ and $^{143}Nd/^{144}Nd = 0.512638 \pm 4$.

Petrography

The biotite-muscovite granite consists of quartz, biotite (some chloritized), muscovite, orthoclase, plagioclase and accessory zircon, ±garnet, apatite, and opaque minerals

(Güleç and Kadioglu 1998; Kadioglu et al. 2003, 2006; Köksal et al. 2007). The hornblende-biotite granite is composed mainly of quartz, hornblende, biotite, orthoclase, plagioclase, with accessory amounts of zircon, titanite, apatite and opaques. Presence of mafic microgranular enclaves, K-feldspar megacrysts, and an abundance of mafic minerals (with hornblende > biotite) are common features in the hornblende-biotite granite (Kadioglu and Güleç 1996).

The granite porphyry dyke shows a porphyritic aphanitic texture with K-feldspar phenocrysts, quartz, biotite, plagioclase, and accessory hornblende, epidote, chlorite, zircon, apatite, and opaques. The alkali feldspar granite has a microgranular texture, and mainly quartz and orthoclase, besides minor amounts of plagioclase, biotite, muscovite, and accessory amounts of chlorite, epidote, zircon, and opaque minerals. The monzonite consists of plagioclase, orthoclase, biotite, hornblende with relict pyroxene cores, quartz, and accessory zircon and titanite (Kadioglu 1996; Kadioglu et al. 2006).

Granitoids in the AIA contain mafic (mainly dioritic) microgranular enclaves that are rounded to subangular to spherical with sharp contacts to their host and finer grained than their host rock (Güleç 1994; Güleç and Kadioglu 1998; Kadioglu and Güleç 1999). These characteristics are interpreted to indicate that magma mingling/mixing processes occurred during evolution of these granitoids (e.g., Didier and Barbarin 1991). Mafic microgranular enclaves exist in all types of granitoids in the AIA, but they are much less abundant in the biotite-muscovite granite than in the other members of the AIA (Kadioglu et al. 2003).

Zircon is found in contact with major phases (biotite, quartz, orthoclase, and plagioclase) and as inclusions within these minerals. Commonly, zircons show microscopically visible zoning and in host biotite often form pleochroic haloes.

Results

Whole-rock geochemistry

The geochemistry of the granitoids within the AIA has been studied in detail by previous authors (e.g., Güleç 1994; Kadioglu and Güleç 1996; Güleç and Kadioglu 1998; Kadioglu et al. 2003, 2006). In addition to available geochemical data, new whole-rock elemental and isotopic geochemical data were obtained from 6 representative samples in the present study (Table 1) to better constrain the general compositional features of these granitoids.

The AIA granitoids show calc-alkaline characteristics, while the hornblende-biotite granite, the granite porphyry and the monzonite are metaluminous, the biotite-muscovite granite and the alkali feldspar granite show metaluminous to peraluminous features (e.g., Kadioglu 1996). The biotite-muscovite granite can be distinguished from other granitoids by its lower SiO_2 but higher TiO_2, Al_2O_3, MgO, P_2O_5 content. Dyke samples (the granite porphyry and the alkali feldspar granite) show higher SiO_2, but lower TiO_2, Al_2O_3, MgO, CaO, P_2O_5, and $Fe_2O_3^{(tot)}$ contents, while the hornblende-biotite granite and the monzonite are intermediate between those. These differences in elemental contents could either be related to the source characteristics, varied abundances of mafic minerals, the temperature conditions, and/or the melting depth in the crust. Based on information obtained from Harker variation diagrams (not shown), Kadioglu (1996) and Güleç and Kadioglu (1998) proposed a fractionation trend from the biotite-muscovite granite to the hornblende-biotite granite, and from the monzonite to the dykes. However, the biotite-muscovite granite and the monzonite samples show rather scattering data and often overlap with the data of the hornblende-biotite granite. The limited major element data confirm that the AIA granitoids as a whole do not represent a single fractionation trend and that the characteristics are a product of source differences as well as later fractionation.

Primitive mantle-normalized multi-element plots for the AIA granitoids, in general, display enrichment in Th, U, K, Pb with negative anomalies in Ba, Nb, Ta, P, and Ti (Fig. 2). Spider plots show a typical crustal signature, but negative Nb and Ti anomalies imply that a distinct subduction component exists in the magma source. This subduction signature is likely to be related to an earlier subduction event in the region, which affected the magma source before generation of the AIA granitoids and the other CAG (e.g., Köksal et al. 2004; Ilbeyli et al. 2004). Chondrite-normalized REE patterns of the AIA granitoids have steep LREE-enriched and almost flat HREE patterns (Fig. 3). The $[La/Yb]_N$ ratios are between 8.63 and 13.47 with concave-upward patterns, suggesting that hornblende was present in the melt fractionation assemblage. Negative Eu-anomalies ($[Eu/Eu^*]_N$) are not very pronounced (0.62–0.78), but imply that plagioclase was another fractionating mineral.

Whole-rock Sr and Nd isotope geochemistry

Strontium and Nd isotope data from the granitoids studied are presented in Table 1. For all samples, $(^{87}Sr/^{86}Sr)_T$ ratios and εNd_T values reveal crustal signatures. All AIA granitoids except the biotite-muscovite granite are represented by Sr and Nd isotopic ratios of very limited range ($[^{87}Sr/^{86}Sr]_T$: 0.70914–0.71027; εNd_T: −6.5 to −7.6) (Table 1), although the alkali feldspar dyke shows slightly higher Sr and lower Nd isotopic ratios than the hornblende-biotite granite, the granite porphyry dyke, and the

Table 1 Whole-rock elemental and Sr and Nd isotope geochemical data from the AIA granitoids

Sample no. Element (wt%)	1 bmg	2 hbg(1)	3 hbg(2)	4 gp	5 afg	6 mz
SiO_2	66.5	70.0	72.3	70.4	76.7	68.1
Al_2O_3	15.2	14.9	13.0	14.5	13.3	14.5
$Fe_2O_3^{tot}$	5.14	3.19	2.65	3.02	2.04	3.62
MgO	2.29	0.76	0.57	0.86	0.11	1.3
CaO	3.11	3.02	2.34	2.52	0.09	3.83
Na_2O	2.17	3.28	2.99	3.31	0.04	2.64
K_2O	3.81	3.83	3.46	4.13	4.1	5.01
TiO_2	0.63	0.24	0.18	0.24	0.13	0.36
P_2O_5	0.12	0.07	0.07	0.05	0.01	0.09
MnO	0.09	0.07	0.08	0.06	<0.01	0.08
Cr_2O_3	0.056	0.064	0.062	0.04	0.025	0.051
LOI	1.2	0.7	2.5	1.2	3.8	0.4
TOTAL	100.3	100.1	100.2	100.3	100.4	100.0
Element (ppm)						
Ba	648	713	451	678	511	478
Sc	14	4	4	4	2	6
Co	13	5	3	6	2	7
Cs	6.0	4.1	3.2	5.6	5.1	11.1
Ga	22	17	14	14	17	17
Hf	5.6	4.1	4	3.7	4.2	5.1
Nb	12	8	10	10	12	15
Rb	145	138	132	156	154	189
Sn	3	2	2	2	4	4
Sr	183	170	186	189	48	467
Ta	0.8	0.7	0.9	1.1	1.3	1.2
Th	16	14	16	18	37	43
U	2.0	3.0	5.3	5.3	6.5	5.4
V	95	31	22	40	32	51
Zr	182	144	122	125	129	171
Y	23	18	18	18	22	23
Cu	34	14	14	18	6	14
Pb	6.1	4.1	3.9	10.9	19.4	25.2
Zn	83	44	41	27	19	34
Ni	45	25	20	28	14	19
La	42	33	33	32	62	49
Ce	82	55	55	54	99	87
Pr	8.2	5.1	5.2	4.8	9.1	8.2
Nd	35.3	19.9	20.0	18.0	33.5	30.1
Sm	6.6	3.4	3.2	3.0	5.3	5.8
Eu	1.2	0.7	0.6	0.6	0.6	1.0
Gd	5.78	3.55	3.17	2.48	4.71	4.56
Tb	0.79	0.48	0.46	0.42	0.64	0.68
Dy	4.0	2.9	2.7	2.5	3.5	3.5
Ho	0.75	0.49	0.48	0.48	0.61	0.64
Er	2.1	1.5	1.6	1.7	2.0	2.1
Tm	0.30	0.23	0.24	0.24	0.30	0.29
Yb	2.4	1.8	1.9	2.1	2.3	2.4
Lu	0.37	0.32	0.29	0.31	0.35	0.38

Table 1 continued

Sample no. Element (wt%)	1 bmg	2 hbg(1)	3 hbg(2)	4 gp	5 afg	6 mz
$^{87}Sr/^{86}Sr$	0.717927 ± 4	0.712307 ± 15	0.711590 ± 4	0.711830 ± 5	0.720031 ± 8	0.710560 ± 5
$^{143}Nd/^{144}Nd$	0.512139 ± 4	0.512234 ± 5	0.512252 ± 3	0.512245 ± 3	0.512197 ± 4	0.512231 ± 3
$(^{87}Sr/^{86}Sr)_T$	0.715191	0.709561	0.709174	0.709143	0.710265	0.709331
εNd_T	−8.84	−6.90	−6.48	−6.70	−7.64	−7.18

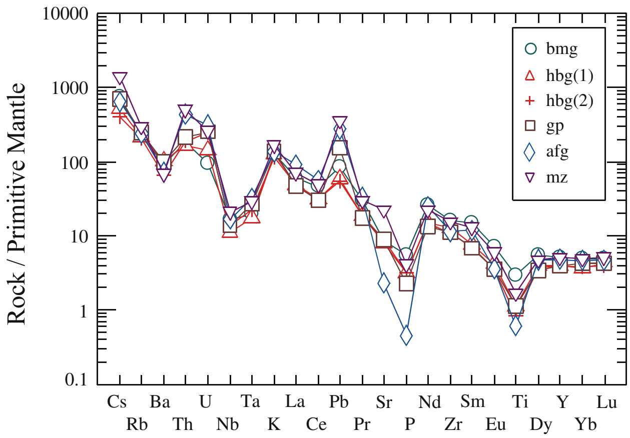

Fig. 2 Primitive mantle-normalized (after Sun and McDonough 1989) trace-element patterns for the AIA granitoids (bmg, the biotite-muscovite granite; hbg, the hornblende-biotite granite; gp, the granite porphyry dyke; afg, the alkali feldspar granite dyke; mz, the monzonite) (data source: Table 1)

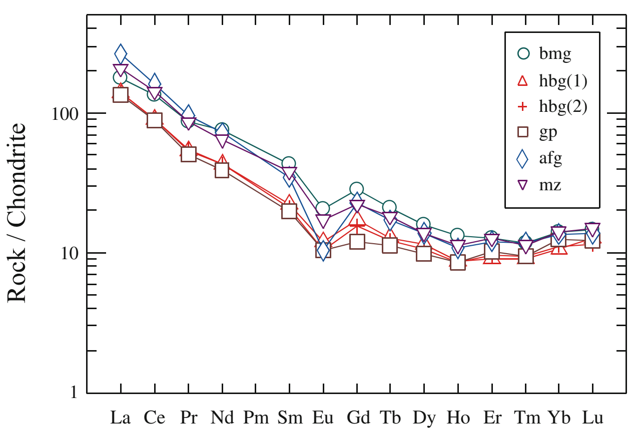

Fig. 3 Chondrite-normalized (after Sun and McDonough 1989) rare-earth element patterns for the AIA granitoids (bmg, the biotite-muscovite granite; hbg, the hornblende-biotite granite; gp, the granite porphyry dyke; afg, the alkali feldspar granite dyke; mz, the monzonite) (data source: Table 1)

monzonite. These isotope data indicate that the magma sources of the AIA granitoids are almost identical, except for the biotite-muscovite granite, which shows more radiogenic Sr isotope ratios and lower εNd_T values than the other granitoids in the area, pointing to an older, more crustal source for this unit. Available Nd and Sr isotope data from some other S-type granitoids in the CACC also have crustal signatures, (e.g., Ilbeyli et al. 2004; Köksal and Göncüoglu 2008) similar to the biotite-muscovite granitoid of the AIA.

Typology and intra-crystalline features of zircons

Studies on crystal habits of zircon provide an approach to a petrogenetic investigation of the granitic rocks (e.g., Pupin 1980; Köksal et al. 2008). Typological and intra-crystalline characteristics of the zircon crystals from the AIA granitoids were studied to identify zircon populations and their growth histories.

Zircon crystals of the biotite-muscovite granite typically show predominant growth of {121} pyramidal face, with {110} ≥ {100}, revealing common S_{12}, S_7, S_2-types, with other rare S- and L-type zircon crystals (Online Resource 3), which is distinctive for S-type granitoids (e.g., Pupin 1980; Schermaier et al. 1992). The other granitoids in the area, on the other hand, have dominant zircon types with {101} ≥ {121} and {100} ≥ {110}, e.g., P-, G- and S_{18}, S_{23}, S_{24}, and other S-type zircon crystals (Online Resource 3), which are characteristic for calc-alkaline hybridized I-type granitic rocks (e.g., Pupin 1980; Schermaier et al. 1992).

CL images of the internal zoning of zircon from the AIA granitoids (Fig. 4), on the other hand, reveal changes in zircon morphology throughout the growth history, and some features not observed from the external morphology may be predominant in the inner parts. The CL images generally show euhedral to subhedral cores, many with near-continuous magmatic overgrowths, but anhedral cores characterized by major breaks in the zoning patterns and interpreted as inherited are not uncommon.

Zircon crystals from the biotite-muscovite granite generally show rounded, inherited, and sometimes metamict cores surrounded by oscillatory zoning with intermittent dissolution surfaces (bmg26, 27, 28 in Fig. 4). The roundness of the cores implies either partial dissolution within the melt or mechanical abrasion during sedimentary transport before its incorporation in the melt (e.g., Paterson et al. 1992). There are also some secondary and later structures such as convolute zoning (flow domains)

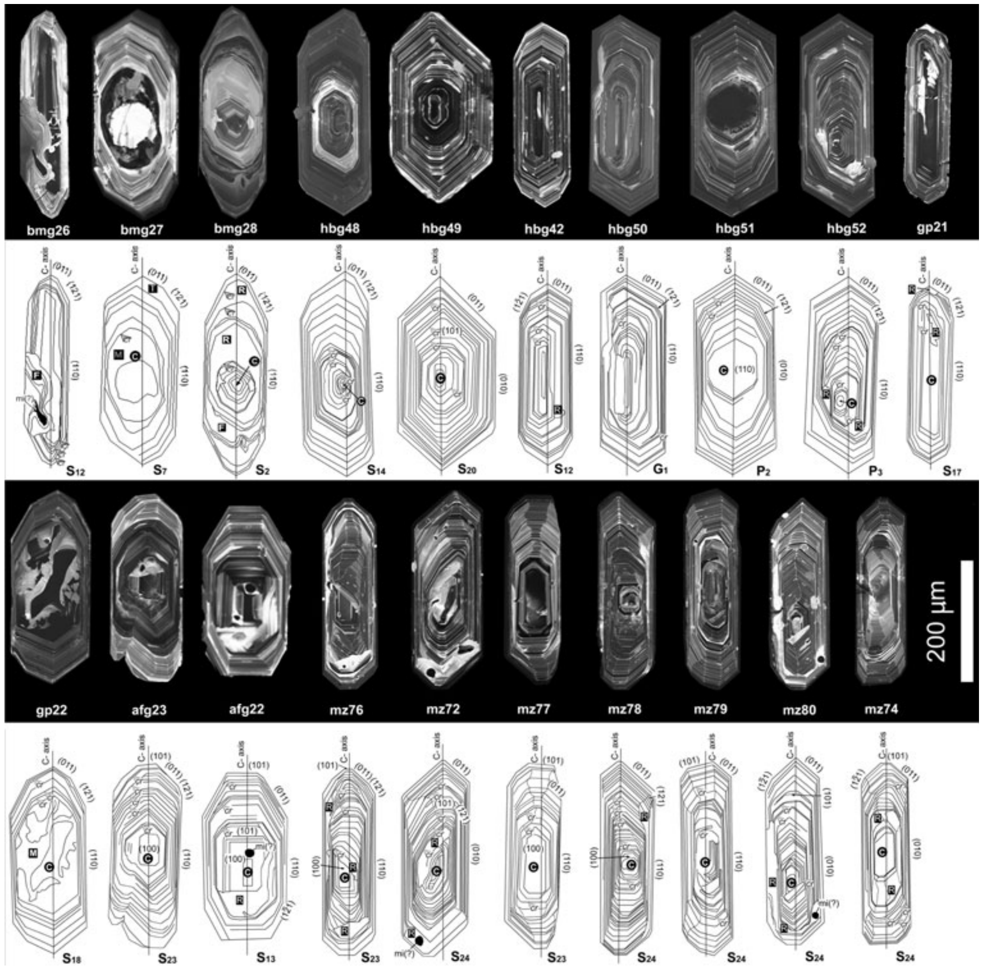

Fig. 4 CL images and sketch models showing the internal structures of the zircon crystals from the AIA granitoids (bmg, the biotite-muscovite granite; hbg, the hornblende-biotite granite; gp, the granite porphyry dyke; afg, the alkali feldspar granite dyke; mz, the monzonite; C, core; R, recrystallized domains or recrystallization patches; F, flow domain; cr, corrosion (resorption or dissolution); T, thickened trace element rich band; M, metamictized domains; mi(?), possible melt inclusion; Ap, apatite inclusion)

overprinting the oscillatory zoning in parts of a zircon, e.g., bmg26 (Fig. 4).

The hornblende-biotite granite is characterized by oscillatory zoned zircon crystals with few inherited cores (Fig. 4). Some crystals (e.g., hbg42 and 50 in Fig. 4) have needle-shaped central zones due to initial skeletal crystal growth indicating high Zr-supersaturation of the melt (e.g., Vavra 1990). In some crystals (e.g., hbg50, 51, 52 in Fig. 4), {121} pyramid surfaces are found in inner parts but progressively less toward the rim, which implies changing chemical conditions during growth. Moreover, intermittent resorption zones from cores to rims imply disruptions of crystal growth.

Zircon crystals of the granite porphyry dyke commonly show inherited and metamict cores surrounded by oscillatory zoning with some corrosion zones (Fig. 4). Outer zones of the crystals are characterized by increasing size of the {121} pyramid, probably because of rapid growth rate of adjacent {011} faces due to adsorption of cations within the magma chamber (e.g., Vavra 1994). Zircons in the alkali feldspar granite dyke, on the other hand, demonstrate oscillatory zoning in grains with low-CL inner and high-CL surrounding parts (Fig. 4). Zircons from the monzonite allow tracing a long history of growth with oscillatory and sector zoning and several intermittent corrosion surfaces (Fig. 4). Rims of the zircon crystals generally show lower-CL brightness than the internal zones. {110}-faces become growth inhibited toward the crystal margins, possibly due to the adsorption of water or trace elements from the magma (e.g., Vavra 1994).

Based on the morphologies and internal structures of zircons studied here, it can be suggested that the inherited cores, which could be an indication of a sedimentary protolith, exist in all granitoid types of the AIA. The intermittent resorption zones disrupting the oscillatory zoning are suggested to be the result of corrosion of zircon grains due to interaction with hotter magma, which is consistent with magma mingling/mixing processes (e.g., Vavra 1994; Köksal et al. 2008).

Geochronology

Selected zircon crystals from the AIA granitoids were dated by U–Pb analysis by LA-SF-ICP-MS. Uranium–Lead ages obtained in this study are presented in Online Resource 1 and BSE images of the selected grains are shown in Fig. 5 and Online Resource 4. Dated grains are different than those imaged by SEM and CL, but reveal similar typological and internal features, i.e., zircon types, inherited cores, and intermittent resorption zones. Inherited cores exist in all granitoid types and their ages range from Proterozoic (e.g., 2,304 ± 70 Ma) through Paleozoic (e.g., 456 ± 16 Ma) to Mesozoic (e.g., 144 ± 9 Ma) (Online Resources 1 and 4, Fig. 5). Some of the zircon cores also yield Late Cretaceous ages, overlapping with the rim ages, and in some cases, these cores are only a few Ma older than the rims (Fig. 5 and Online Resource 4). Rims and outer zones of zircons from the AIA granitoids give Late Cretaceous ages, from 71 ± 2 to 86 ± 3 Ma. The data used here are $^{206}Pb/^{238}U$ ages when the concordance level is more than 90%, and $^{207}Pb/^{206}Pb$ ages if the U–Pb analyses are discordant (less than 90% concordant) (Online Resource 1). Most Late Cretaceous ages are concordant or near concordant, while the discordant ages were mostly found in inherited cores. Combining the U–Pb data with the SEM, CL, and BSE images, we conclude that there was a Late Cretaceous event in which the older zircon crystals were resorbed and recrystallized, and new zircon crystals grew.

Concordia plots together with the mean or median $^{206}Pb/^{238}U$ ages are presented in Fig. 6. Whenever possible, i.e., MSWD values are close to 1, mean $^{206}Pb/^{238}U$ ages are given, median ages are presented in the other cases. The biotite-muscovite granite gives a mean $^{206}Pb/^{238}U$ age of 84.1 ± 1.0 Ma (Fig. 6a). The hornblende-biotite granite, on the other hand, has a median $^{206}Pb/^{238}U$ age of 82.3 + 0.8/−1.1 Ma (Fig. 6b). Median $^{206}Pb/^{238}U$ ages of the granite porphyry dyke and the alkali feldspar dyke are 79.1 + 2.1/−1.5 and 75.0 + 1.0/−1.0 Ma, respectively (Fig. 6c, d). Uranium–Lead concordia age (6 points), i.e., 74.9 ± 0.8 Ma (95% conf.), of the alkali feldspar dyke is so close to the median age (not shown). The monzonite gives a mean $^{206}Pb/^{238}U$ age of 73.6 ± 0.4 Ma (Fig. 6e). Excess scatter is interpreted to be related to minor inherited components, which shift the analytical data toward higher $^{207}Pb/^{235}U$, $^{206}Pb/^{238}U$, and $^{207}Pb/^{206}Pb$ ages. Only results that are more than 90% concordant are incorporated in the calculation of averages and those data points are shown in bold outline in the figures. Based on these ages, it can be deduced that the biotite-muscovite granite and the hornblende-biotite granite are the oldest intrusions in the area. The mean $^{206}Pb/^{238}U$ age of the biotite-muscovite granite is ca. 1 Ma older than that of the hornblende-biotite granite, but their ages overlap within analytical error. The monzonite and the alkali feldspar granite dyke are significantly younger than the other granitoids in the Agaçören area (Fig. 6). In brief, U–Pb data of the AIA granitoids collectively document continuous granitic

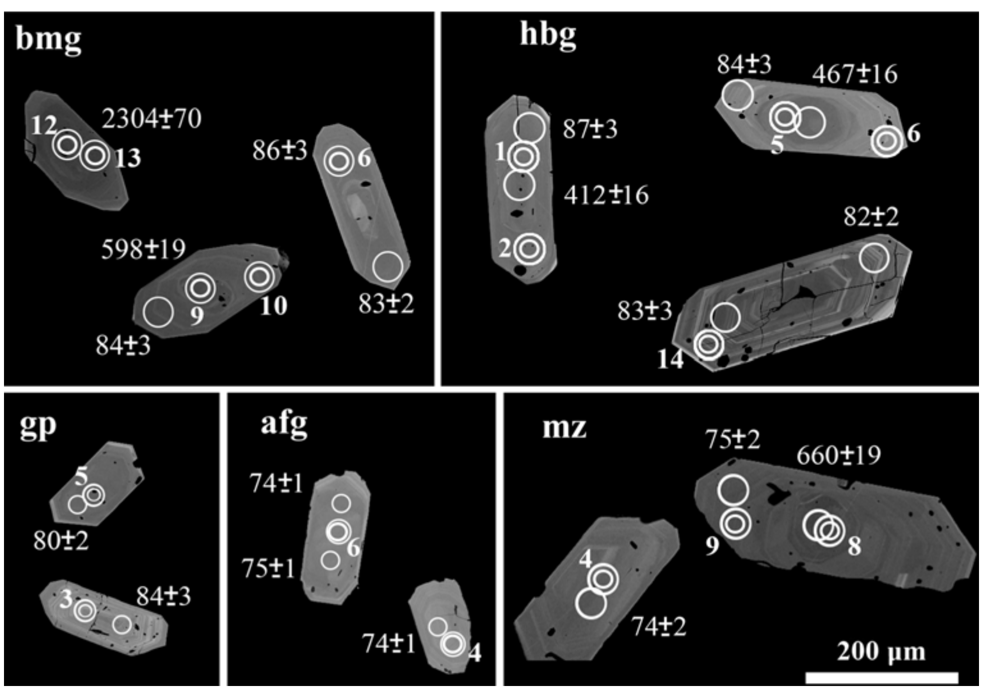

Fig. 5 Selected BSE images and the LA-SF-ICP-MS U–Pb ages (in Ma) of the zircon crystals from the biotite-muscovite granite (bmg), the hornblende-biotite granite (hbg), the granite porphyry dyke (gp), the alkali feldspar granite dyke (afg), and the monzonite (mz). LA spot diameter is ca. 40 µm in bmg, hbg, and mz, and ca. 30 µm in gp and afg. *Double circles* (ca. 40 µm) with numbers indicate the locations of the LA-MC-ICP-MS Lu–Hf isotope analyses (Full version of this figure can be found as Online Resource 4)

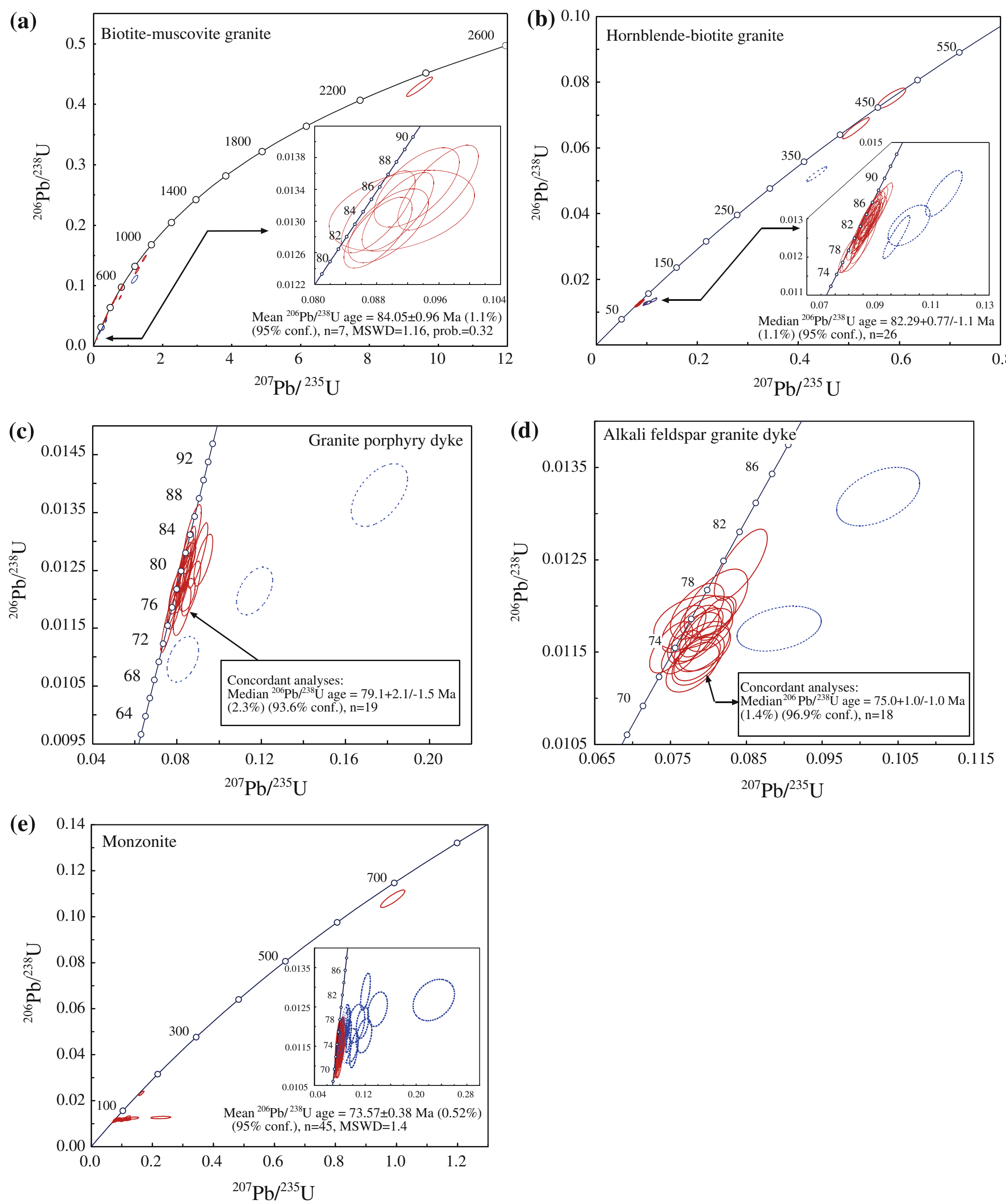

Fig. 6 Concordia plots with mean $^{206}Pb/^{238}U$ ages based on the LA-SF-ICP-MS U–Pb zircon analyses from **a** the biotite-muscovite granite, **b** the hornblende-biotite granite, **c** the granite porphyry dyke, **d** the alkali feldspar granite dyke, **e** the monzonite

intrusion between 84 and 74 Ma. However, the most voluminous granitic magmatic activity may be constrained to within two main periods, i.e., older biotite-muscovite and hornblende-biotite granite intrusions at 84–82 Ma, and the monzonite intrusion at 74 Ma. The formation of the alkali feldspar and the granite porphyry dykes in between these main periods is evidence for continuous magmatic activity in the area.

Zircon Lu–Hf isotopic characteristics

In situ Lu–Hf isotope analyses were carried out on 57 zircons from various granitoid types of the Agaçören pluton and results are presented in Table 2, as well as in Figs. 7, 8 and in the Online Resources 2, 5, 6. The Lu–Hf analyses have been performed at the same analyses spots or from the same growth domains where U–Pb ages were determined; hence, it is possible to correlate Lu–Hf isotopic data with ages (Fig. 5). The lowest and highest $^{176}Hf/^{177}Hf_{(t)}$ ratios are found to be 0.28095 (in the biotite-muscovite granite) and 0.28268 (in the monzonite), respectively (Table 2 and Online Resources 2 and 5). The lowest $^{176}Hf/^{177}Hf_{(t)}$ data correspond to the oldest ages obtained from the AIA zircons, consistent with reworking of old crustal material. Two zircon cores with the Early Proterozoic ages reveal slightly lower $\varepsilon Hf_{(t)}$ values compared with the data reported from the Lewisian granulites (Whitehouse and Kemp 2010), south African gneisses/granitoids (Zeh et al. 2007; Millonig et al. 2010), Armonican metasedimentary rocks (Gerdes and Zeh 2006), and Gondwanan detrital zircons (Kemp et al. 2006) (Fig. 8), but lie on a similar crustal trend toward Archean mantle extraction. These two data points are evidence for a small proportion of very old crustal material in the source of the AIA granitoids. A relative probability plot of the U–Pb ages combined with $\varepsilon Hf_{(t)}$ (Fig. 7) shows that $\varepsilon Hf_{(t)}$ decreases toward younger ages, starting from ca. 600 Ma, which represent decreasing mantle contribution besides a significant crustal component (Fig. 7). Analyses with Paleozoic crystallization ages spread between $\varepsilon Hf_{(t)}$ −6.6 and −0.3, which most likely represents crustal reworking during that time. The wide range of Lu–Hf isotope data of the inherited zircon suggests heterogeneous sources for the AIA granitoids. However, when only the Late Cretaceous zircon domains are considered, the $^{176}Hf/^{177}Hf_{(t)}$ ratios of all granitoids are restricted to a more restricted range, between 0.28247 and 0.28260, compared with Hf isotope range of older zircon domains (Online Resource 5, inset diagrams), corresponding to $\varepsilon Hf_{(t)}$, of −4.1 to −8.8. This variation (−6.2 ± 2.3) is only about twice the reproducibility (ca. ±1 εHf) of the method. The relative homogeneity of the Lu–Hf isotope system in the different AIA granitoids can be also observed in the $\varepsilon Hf_{(t)}$ against $^{176}Lu/^{177}Hf$ diagrams for Cretaceous zircon domains (Online Resource 6). Thus, the variable ages and Hf isotope composition of inherited zircon are consistent with melting of heterogeneous crustal material during generation of AIA granitoids. During magma genesis, this material was mixed and homogenized leading to various intrusions having very similar isotopic composition. The homogeneity of the Late Cretaceous Lu–Hf isotope data of the CAG is apparent when compared with the data from different regions of the world, such as the East Asian (Griffin et al. 2002; Chu et al. 2006; Zheng et al. 2007; Zhong et al. 2009; Qin et al. 2010) and Australian granitoids (Kemp et al. 2007) (Fig. 8). A narrow range of Hf isotope ratios was reported by Siebel and Chen (2010) for the SW Bohemian granitoids (Fig. 8), but these data range from positive to negative $\varepsilon Hf_{(t)}$ values indicating the presence of both enriched and depleted mantle material and crustal components in these rocks (Siebel and Chen 2010).

Discussion and conclusions

The age and formation of the granitoids in the Agaçören area are investigated in this study using U–Pb and Hf isotope systematics. The data presented establish that AIA granitoids with differing composition were formed during the Late Cretaceous between 84 and 74 Ma. The mineralogical, geochemical, and geochronological data are consistent with a multi-stage magmatic evolution of the granitoids in central Anatolia (e.g., Kadioglu et al. 2006; Köksal and Göncüoglu 2008; Boztug and Harlavan 2008). The generation of S- and I-type granitoids at ca. 84–82 Ma was followed by minor I-type granitic activity, characterized by dykes and small intrusions, up to ca. 74 Ma, when the voluminous I-type monzonitic intrusions together with coeval A-type granitoids formed (e.g., Köksal et al. 2004; Ilbeyli et al. 2004). Previously determined geochronological data have to be discussed in relation to the results of this study for their consistency with this interpretation. An $^{40}Ar/^{39}Ar$ biotite age of 77.6 ± 0.3 Ma from the biotite-muscovite granite within the AIA reported by Kadioglu et al. (2003, 2006) may be related to cooling from regional metamorphic conditions considering our mean $^{206}Pb/^{238}U$ zircon age of 84.1 ± 1 Ma from the same unit. Köksal et al. (2007) presented a mean $^{206}Pb/^{238}U$ zircon age of 83.8 ± 1.0 Ma for the biotite-muscovite granite, and similar pre-80 Ma ages were obtained from other two-mica granitoids from different parts of the CACC. These are the Sinandi granitoid (Fig. 1) with an 81.5 ± 0.8 Ma mean LA-SF-ICP-MS $^{206}Pb/^{238}U$ zircon age (Köksal et al. 2007) and the Danaciobasi granitoid (Fig. 1) with an 87 ± 9 Ma $^{207}Pb/^{206}Pb$ zircon evaporation age (Boztug et al. 2007b). The age of the Uçkapili granitoid (Fig. 1) was determined as 77.8 ± 1.2 Ma by a combined whole-rock, biotite and muscovite Rb–Sr isochron and cooling ages of 78.5 ± 1.2 to 74.9 ± 1.2 Ma by the K–Ar method were obtained on biotite and muscovite by Göncüoglu (1986). The U–Pb age for the hornblende-biotite granite of 84.1 ± 1 Ma of the AIA presented here is identical within error to that of biotite-muscovite granite, i.e., $^{206}Pb/^{238}U$ age of 82.3 + 0.8/−1.1 Ma. Age data from hornblende-bearing granitoids in other parts of the CACC (see Fig. 1) were presented for the Behrekdag batholith as a 79.5 ± 1.7 Ma K–Ar hornblende age (Ilbeyli et al. 2004), for the Kerkenez granitoid as a 81.2 ± 0.5 Ma $^{40}Ar/^{39}Ar$ hornblende age (Isik et al. 2008), and for the Akçakoyunlu granitoid as 79.3–77.6 Ma K–Ar hornblende ages (Boztug et al. 2007c), all to be interpreted as cooling ages. Therefore, it is plausible to suggest that the Late Cretaceous magma generation within the CACC

Table 2 Selected LA-MC-ICP-MS Lu–Hf isotope data of zircons from the AIA granitoids (Full version of this table can be found as Online Resource 2)

Analysis No.	$^{176}Yb/^{177}Hf$[a]	±2σ	$^{176}Lu/^{177}Hf$[a]	±2σ	$^{178}Hf/^{177}Hf$	$^{180}Hf/^{177}Hf$	SigHf[b] (V)	$^{176}Hf/^{177}Hf$	±2σ	$^{176}Hf/^{177}Hf_{(t)}$	$\varepsilon Hf^{c}_{(t)}$	±2σ	T^{d}_{DM2} (Ga)	age[e] (Ma)	±2σ
Biotite-muscovite granite															
1	0.0144	17	0.00036	4	1.46713	1.88670	21	0.282448	18	0.282446	−4.4	0.6	1.44	324	9
4	0.0552	25	0.00145	6	1.46724	1.88698	19	0.282511	19	0.282509	−7.5	0.7	1.41	84	3
9	0.0461	31	0.00131	14	1.46730	1.88703	16	0.282477	22	0.282462	2.2	0.8	1.30	598	19
13	0.0193	18	0.00057	6	1.46715	1.88670	17	0.280977	19	0.280953	−12.8	0.7	3.50	2304	70
Hornblende-biotite granite															
2	0.0617	15	0.00162	7	1.46718	1.88682	22	0.282505	18	0.282503	−7.6	0.6	1.42	87	3
5	0.0156	7	0.00042	2	1.46708	1.88684	13	0.282455	18	0.282452	−1.0	0.6	1.37	467	16
11	0.0491	27	0.00138	8	1.46723	1.88687	16	0.282579	18	0.282577	−5.1	0.6	1.28	82	3
11b[f]	0.0491	27	0.00138	8	1.46723	1.88687	16	0.282579	18	0.282577	−5.1	0.6	1.28	82	3
Granite porphyry dyke															
3	0.0556	33	0.00166	8	1.46717	1.88674	20	0.282586	17	0.282583	−4.8	0.6	1.27	84	3
5	0.0631	22	0.00168	6	1.46713	1.88670	14	0.282501	20	0.282498	−7.9	0.7	1.44	80	2
Alkali feldspar granite dyke															
4	0.0371	16	0.00108	4	1.46719	1.88680	14	0.282544	18	0.282543	−6.5	0.6	1.35	74	1
6	0.0345	48	0.00101	12	1.46724	1.88689	16	0.282585	18	0.282584	−5.0	0.7	1.27	74	1
Monzonite															
1	0.0172	23	0.00050	6	1.46710	1.88687	16	0.282505	18	0.282505	−7.9	0.6	1.43	73	2
2	0.0644	9	0.00170	3	1.46717	1.88678	12	0.282685	20	0.282681	0.0	0.7	1.06	148	5
4	0.0446	8	0.00129	2	1.46724	1.88689	21	0.282569	16	0.282568	−5.6	0.6	1.30	74	2
8	0.1020	37	0.00236	13	1.46713	1.88674	9	0.282374	26	0.282344	−0.6	0.9	1.50	660	19
GJ-1[g], $n = 11$	0.0104	94	0.00031	8	1.46721	1.88685	19	0.282005	13	0.282002	−13.8	0.5	2.19	609	9

[a] $^{176}Yb/^{177}Hf = (^{176}Yb/^{177}Hf)_{true} \times (^{173}Yb/^{177}Hf)_{meas} \times (M_{176(Yb)}/M_{173})^{\beta(Yb)}/(M_{176(Yb)}/M_{177})^{\beta(Yb)}$ (Hf). $^{176}Lu/^{177}Hf$ values were calculated in a similar way by using the measured $^{175}Lu/^{177}Hf$ and the β_{Yb}. The effect of the inter-element fractionation on the Lu/Hf was estimated to be 4–6%. [b] Mean Hf signal in volt. [c] Calculated using a decay constant of 1.865×10^{-10} (Scherer et al. 2001), a CHUR $^{176}Lu/^{177}Lu$ and $^{176}Hf/^{177}Hf$ ratio of 0.0332 and 0.282772, and the ages obtained by LA-ICP-MS. [d] Two stage model age using the measured $^{176}Lu/^{177}Lu$ of each spot (first stage = age of zircon), a value of 0.0113 for the average continental crust (second stage), and a depleted mantle $^{176}Lu/^{177}Lu$ and $^{176}Hf/^{177}Hf$ of 0.0384 and 0.28325, respectively. [e] U–Pb or Pb–Pb preferred zircon ages (data source Online Resource 1). [f] Replicate analysis. [g] Mean ± 2σ SD of 11 spot analyses of GJ-1 reference zircon

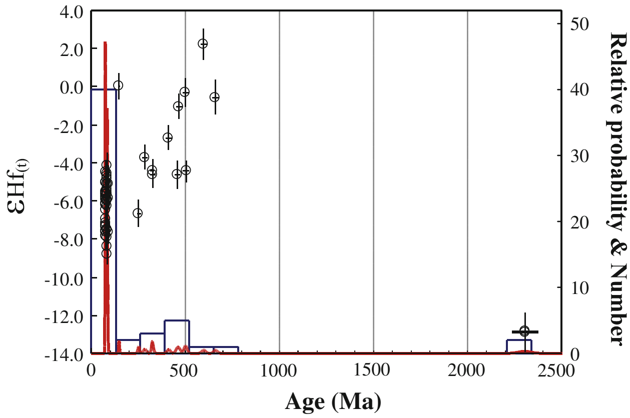

Fig. 7 Relative probability diagram combined with $\varepsilon Hf_{(t)}$ versus age (Ma) diagram from the AIA granitoids (Data source Online Resources 1 and 2)

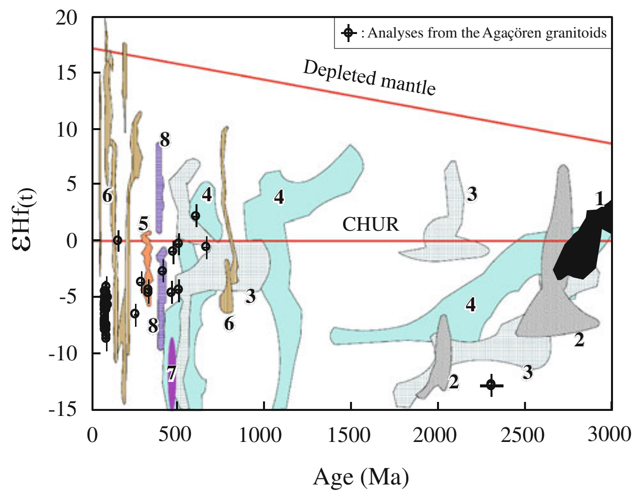

Fig. 8 Comparison of the Lu–Hf isotope data of the AIA (open circles with error bars) with those of the other rocks from different regions from the world. *1* Lewisian granulites (Whitehouse and Kemp 2010), *2* Gneisses and granitoids from South Africa (Botswana) (Zeh et al. 2007; Millonig et al. 2010), *3* Detrital zircons from Armorican metasediments (Gerdes and Zeh 2006), *4* Gondwanan detrital zircon data (Kemp et al. 2006), *5* SW Bohemian Granitoids (Siebel and Chen 2010), *6* Granitoids from East Asia (Griffin et al. 2002; Chu et al. 2006; Zheng et al. 2007; Zhong et al. 2009; Qin et al. 2010), *7* S-type granitoids from Scottish Caledonides (Appleby et al. 2010), *8* Australian igneous rocks (Kemp et al. 2007). *DM line* is from Griffin et al. (2000)

forming the biotite-muscovite and hornblende-biotite granitoids had crystallization ages between 84 and 82 Ma and cooling ages of 81–77 Ma. Whitney et al. (2003) described the age of the Uçkapili granitoid as 92–85 Ma based on their U–Pb SHRIMP zircon ages. Their data (Table 3 in Whitney et al. 2003), on the other hand, show a mean $^{206}Pb/^{238}U$ age of 83.9 ± 2.4 Ma (at 95% CI; excluding the point with 66.5 ± 0.5 Ma), which is consistent with our data. Accordingly, the $^{40}Ar/^{39}Ar$ age of 79.4 ± 1.0 Ma determined by those authors is also consistent with our interpretation as a cooling age.

There are younger dykes within the AIA, i.e., the granite porphyry dyke with 79.1 + 2.1/−1.5 Ma and the alkali feldspar dykes with 75.0 + 1.0/−1.0 Ma ages indicating that magmatism is continuous in this period. However, the second main magma generation event in the area is monzonitic. The mean $^{206}Pb/^{238}U$ age obtained on the monzonite is 73.6 ± 0.4 Ma, consistent with the ages of other monzonitic rocks within central Anatolia. These monzonitic granitoids in the CACC are the Cefalikdag granitoid (Fig. 1), which yielded a 73.5 ± 1.0 Ma Rb–Sr whole-rock age (Ataman 1972) and a 70.0 ± 1.0 Ma $^{40}Ar/^{39}Ar$ amphibole and biotite age by Kadioglu et al. (2006); the Baranadag granitoid (Fig. 1) with a 74.0 ± 2.8 Ma U–Pb titanite age by Köksal et al. (2004), a 76.4 ± 1.3 Ma K–Ar hornblende age by Ilbeyli et al. (2004), and a 74.1 ± 4.9 Ma $^{207}Pb/^{206}Pb$ zircon evaporation age by Boztug et al. (2007b); the Kerkenez granitoid with a 72.6 ± 0.2 Ma $^{40}Ar/^{39}Ar$ hornblende age by Isik et al. (2008), and the Adatepe and the Yassiagil granitoids (Fig. 1) with 79.8–68.0 Ma K–Ar cooling ages by Boztug et al. (2007c). We interpret these results to date monzonitic magmatism in central Anatolia at ca. 74 Ma with a cooling period from 71 to 68 Ma.

There is a third episode of magmatism coeval or younger than the monzonitic phase, including A-type syenitic and foid-syenitic granitoids in the CACC, e.g., the Çamsari granitoid (Fig. 1) with a U–Pb titanite age of 74.1 ± 0.7 Ma (Köksal et al. 2004) and the Bayindir granitoid (Fig. 1) with 69.8 ± 0.3 Ma $^{40}Ar/^{39}Ar$ amphibole and biotite ages (Kadioglu et al. 2006). In contrast, Boztug et al. (2007b) suggested the presence of Mid-Cretaceous A-type CAG, e.g., the Konur granitoid with an age of 92.4 ± 5.6 Ma, the Çamsari granitoid (95.7 ± 5.1 Ma), the Çayagzi granitoid (97.0 ± 12.0 Ma), and the Karaçayir granitoid (99.0 ± 11.0 Ma). Their interpretation, based on $^{207}Pb/^{206}Pb$ zircon evaporation analyses, contradicts field observations in the CACC and also their $^{40}Ar/^{39}Ar$ ages of ca. 67–65 Ma, which would indicate an unlikely slow post-crystallization cooling period. It can be argued that the presence of inherited cores within the zircon grains disturbed the $^{207}Pb/^{206}Pb$ zircon evaporation results (e.g., Göncüoglu 2009). Such inheritance structures in the zircons of the Çamsari granitoid have been also demonstrated recently by Köksal et al. (2008).

Whole-rock element and Sr and Nd isotope geochemical data show that the granitoids in the Agaçören area have crustal source characteristics, i.e., enrichment in Th, U, K, Pb with $(^{87}Sr/^{86}Sr)_T$ ratios >0.708 and low εNd_T values, but it is difficult to identify a single fractionation trend with the available data. The geochemical data rather infer different source characteristics for the subunits of the AIA. The biotite-muscovite granite shows a more pronounced crustal signature, higher Sr and lower Nd isotopic ratios, but its crystallization age is similar to that of the hornblende-biotite granite. This can be explained either by formation of the biotite-muscovite granite several million years before the hornblende-biotite granite (taking the error envelope of the ages into account) from a different source or by formation of coeval biotite-muscovite and hornblende-biotite granitoids from different domains (or from different depths) within the crust. The younger intrusions, especially the monzonite in the AIA, are likely to have additional components in their genesis but they may be related to the slightly earlier granitoids by assimilation-fractional crystallization (AFC) processes. The geochemical data from the AIA are limited, but similar monzonitic granitoids within the CACC are interpreted to be derived from crustal sources and/or enriched lithospheric mantle accompanied by crustal contamination processes (e.g., Köksal et al. 2004; Ilbeyli et al. 2004; Boztug et al. 2007a).

There are geodynamic models linking the evolution of the CAG to the Inner Tauride Ocean, proposed as an ocean separating the CACC from the Tauride-Anatolide microplate (e.g., Sengör and Yilmaz 1981; Görür et al. 1984, 1998; Whitney and Dilek 1997; Kadioglu et al. 2003, 2006). In these models, the CAG are either related to Andean-type calc-alkaline arc magmatism occurring during closure of the Inner Tauride Ocean in Early Paleocene-Eocene times by northward subduction beneath the CACC (e.g., Sengör and Yilmaz 1981; Görür et al. 1984, 1998). Alternatively, the CAG are related to syn-collisional magmatism due to the collision and partial subduction of the leading edge of the Tauride micro-plate with a trench in the Inner Tauride ocean and subsequent slab break-off (e.g., Kadioglu et al. 2006).

Another alternative model, which we favor, is to interpret the CAG as collisional and post-collisional granitoids formed within the northern passive margin of the Tauride-Anatolia microplate (Fig. 9a), i.e., the CACC, subsequent to the closure of the northern branch of the Neotethyan Ocean along the IAESZ (e.g., Göncüoglu et al. 1991; Akiman et al. 1993; Yaliniz et al. 1999, 2000; Boztug 2000; Düzgören-Aydin et al. 2001). In this model, MORB-type oceanic crust, together with the OIB-type volcanic rocks and accretion prism material, was obducted onto the passive margin of the Tauride-Anatolide microplate during the Middle Cretaceous. This resulted in the formation of ophiolitic-nappes giving way to crustal thickening at the passive CACC margin (Fig. 9b, c). The thickening of the CACC crust first resulted in high temperature–low pressure regional metamorphism, and then, coeval or post-metamorphic collisional granitoids were formed probably from the tonalitic source (e.g., Erler and Göncüoglu 1996; Yaliniz et al. 2000) (Fig. 9c). A crustal source of the 84–82 Ma granitoids within the AIA as interpreted from the geochemical and Sr, Nd, and Hf isotopic data is consistent with this interpretation. The generation of these granitoids has probably triggered extension and rapid exhumation (Whitney et al. 2003; Isik et al. 2008) that resulted in decompressional melting of the middle crust (Whitney et al. 2003). Agreement of the ages of the granitoids (i.e., ca. 84–82 Ma) with the age of peak metamorphism (Göncüoglu 1986; Floyd et al. 2000; Whitney et al. 2003) manifests a direct link between the regional metamorphism and the widespread collisional S- and I-type granitic magmatism in central Anatolia. These large-scale metamorphic and magmatic events during this period probably caused also crustal homogenization within the CACC (Fig. 9c). During this period, intraoceanic subduction and ensimatic island arcs were formed. Trench rollback formed through subduction of the forearc basin and gave rise to extension within the oceanic crust and formation of supra-subduction zone (SSZ) ophiolites (e.g., Yaliniz et al. 2000; Floyd et al. 2000) in the Izmir-Ankara oceanic lithosphere to the north (Fig. 9b, c).

The convergent regime that continued during the Late Cretaceous is characterized by obduction of the dismembered SSZ-ophiolites and collision of an ensimatic island arc with the CACC margin (e.g., Yaliniz et al. 2000) (Fig. 9d). Post-collisional uplift and extension followed the complete obduction of the SSZ-ophiolites. The age of this episode can be constrained by the U–Pb age of the monzonite (i.e., ca. 74 Ma) from the AIA and similar monzonitic granitoids from the CACC (e.g., Ilbeyli et al. 2004; Köksal et al. 2004). The predominantly crustal signature of the monzonite inferred from geochemical and Sr, Nd, Hf isotope data is related to either crustal melting or enriched mantle sources. Accordingly, these monzonitic I-type CAG of ca. 74 Ma age, together with some A-type granitoids, are interpreted to be related to melting of lower crustal granitic and granulitic rocks, residual material from the older metamorphic and magmatic events, and probably the subcontinental lithospheric mantle rocks with heat supplied by mantle-derived mafic magma underplating of the lower crust as a result of lithospheric delamination and thinning (e.g., Göncüoglu and Türeli 1994; Aydin et al. 1998; Boztug 1998, 2000; Düzgören-Aydin et al. 2001; Köksal et al. 2004; Ilbeyli et al. 2004; Boztug et al. 2007a, b, c; Boztug and Arehart 2007; Boztug and Harlavan 2008; Boztug et al. 2009) in this post-collisional period (Fig. 9d). The hybrid magma source that is indicated by the abundant mafic microgranular enclaves within the CAG is suggested to be the result of interaction of the underplating magma with the base of the crust as argued by Voshage et al. (1990).

Extension continued in the late Campanian–early Maastrichtian and was characterized by the formation of the

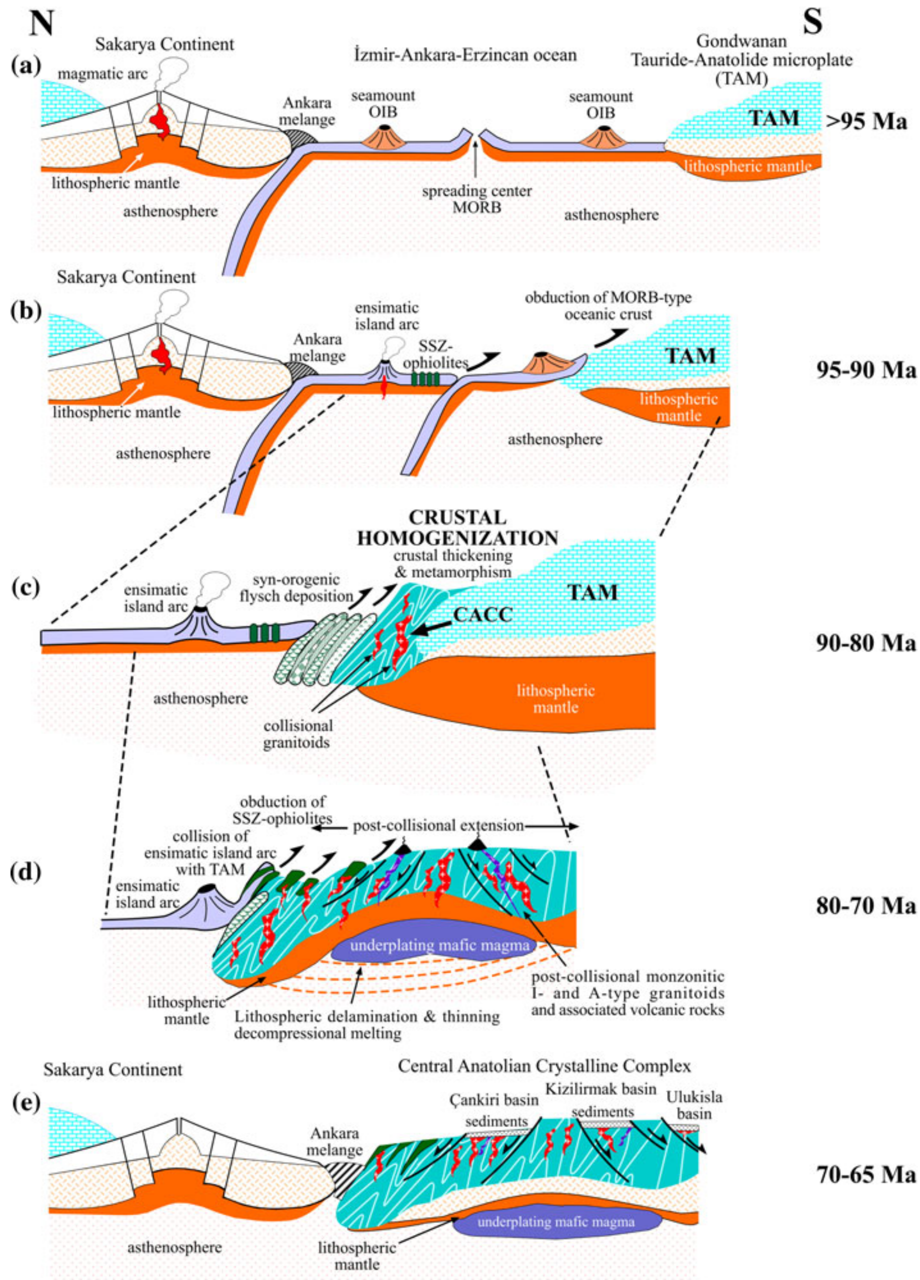

Fig. 9 Schematic representation of the proposed model for the tectonic evolution of the CACC in the Late Cretaceous

silica-saturated to undersaturated A-type granitoids and associated volcanic rocks (e.g., Boztug 2000; Köksal et al. 2001; Boztug and Arehart 2007). The post-collisional thickening period in central Anatolia ended with formation of A-type granitoids (e.g., Köksal et al. 2004) and changed into an extensional regime, characterized by alkaline volcanic rocks (Köksal et al. 2001; Alpaslan et al. 2004, 2006; Kurt et al. 2008), while the Sakarya Continent was juxtaposed to the CACC with the Ankara mélange in between those units (Fig. 9e). Last stage granitoids in the CACC cooled and were exhumed during the Early to Middle Paleocene (Boztug et al. 2008). This was concurrent with the formation of the central Anatolian foreland basins (Göncüoglu et al. 1991) (Fig. 9e).

Evidences for these complex geological processes from the Early Proterozoic to the pre-Late Cretaceous are the U–Pb ages and the Lu–Hf isotope data of zircons from the AIA granitoids. Zircon crystals with inherited cores also display the crustal-derived nature of the granitoids. These cores mostly gave Proterozoic ages, also documented from the granitic and metamorphic rocks in the Nigde area by U–Pb SHRIMP zircon analyses of Whitney et al. (2003). In addition, the zircon Lu–Hf isotope data of Paleozoic age from the AIA granitoids are close to those of Gondwanan detrital zircons (Kemp et al. 2006). These features can be interpreted as evidence for a Gondwanan origin of the CACC, which is the topic of another study (Göncüoglu et al. in prep). There is a correlation of the Lu–Hf isotope data with some of the Variscan rocks of Paleozoic age (e.g., SW Bohemian Granitoids, Siebel and Chen 2010) (Fig. 8), which show a similar spread in $\varepsilon Hf_{(t)}$ values than the AIA granitoids, but more CHUR-like values. Many inherited zircon cores were corroded, by mechanical abrasion or possibly during the subsequent magmatic stages by dissolution during influx of hot juvenile magma. More juvenile magma generation in the Neoproterozoic is consistent with some of the Lu–Hf isotope data, whereas Hf isotopic data for the Late Cretaceous granitoids are very homogeneous and the low $\varepsilon Hf_{(t)}$ values are consistent with crustal isotopic characteristics of the AIA granitoids.

The main general conclusion of this study is that the crustal origin and strong heterogeneity of the source material can be traced by in situ U–Pb geochronology, whereas the Lu–Hf data show that there is very effective homogenization of this isotopic system during the regional metamorphic and magmatic events in the Late Cretaceous. The inherited zircon grains are evidence for strong age and isotopic heterogeneity of the reworked crust. However, Lu–Hf isotope data of Cretaceous zircon domains from different granitoids in the Agaçören area indicate a relative homogeneous isotope composition of the crustal melts. This circumstance may be explained by the homogenization and mixing of the heterogeneous pre-Cretaceous crust during the high temperature (up to 725°C; Whitney et al. 2003) metamorphic conditions and syn- or post-metamorphic magmatic activity in central Anatolia in the Late Cretaceous. Effective homogenization of the isotopic system is interpreted to have caused the observed restricted Hf isotopic data for the first phase of the AIA granitoids. Younger intrusions within the AIA picked up this isotopic nature of the pre-existing crust during their formation via assimilation and fractional crystallization processes. Similar isotopic homogenization of the crust was also reported by Millonig et al. (2010) from the Mahalapye complex (Botswana), where a high-grade tectonometamorphic overprint was accompanied by magmatic intrusions. Their interpretation is that Hf isotopic homogenization was likely to have occurred during granitic melting formed from a crustal source at or immediately after the metamorphic peak. Crustal homogenization in the AIA studied here can also be inferred from the relatively homogeneous chemical composition of the granitoids with only minor chemical differences. However, for the genesis of the AIA granitoids, an involvement of enriched lithospheric source material cannot be ruled out by the available data. The range of the Hf isotopic data for the S-type post-tectonic granitoids from the Scottish Caledonides (Fig. 8) is also very narrow, but zircon oxygen isotope data reveal heterogeneity in the source (Appleby et al. 2010). Future research on oxygen isotope systematics of zircon from the AIA granitoids and Hf isotopic studies on the pre-Cretaceous basement of central Anatolia should be able to resolve these issues, but are beyond the scope of the present study.

In addition to chemical and isotopic homogenization, extensive metamorphism and following physical processes recorded within the central Anatolian crust, e.g., extension of the middle to upper crust and lateral underflow of the lower crust (Whitney et al. 2003; Gautier et al. 2008), might also have resulted in mechanical homogenization of the central Anatolian crust. Alternatively, the extent of the crustal homogenization (i.e., complete or partial) remains an open question, since the whole-rock Sr and Nd isotopic character of the biotite-muscovite granite is significantly different from the other granitoids in the area. The scale of the crustal homogenization may be tested in future studies on zircon from the other igneous associations, including younger granitic and volcanic rocks within the CACC, to complete the crustal evolution scenario.

Acknowledgments We wish to thank the Scientific and Technical Research Council of Turkey (TUBITAK; project codes 101Y051 and 106Y066) for supporting the whole-rock geochemical and LA-ICP-MS U–Pb analyses. We acknowledge Radiogenic Isotope Laboratory of Middle East Technical University Central Laboratory for Sr–Nd isotope analyses, Johann Wolfgang Goethe Universität, Institut für Geowissenschaften for zircon Lu–Hf isotope analyses and GFZ-Potsdam for accessing to SEM and CL imaging. We thank Pinar Tokmakkaya for her assistance with the radiogenic isotope analyses and Fatma Toksoy-Köksal for her comments on the petrographical and geochemical interpretations. We would like to thank K. Mezger, W. Siebel and an anonymous reviewer for their constructive comments and suggestions, and J. Hoefs for editorial handling and patience with the revisions.

References

Akiman O, Erler A, Göncüoglu MC, Güleç N, Geven A, Türeli K, Kadioglu YK (1993) Geochemical characteristics of granitoids along the western margin of the Central Anatolian Crystalline Complex and their tectonic implications. Geol J 28:371–382

Alpaslan M, Frei R, Boztug D, Kurt MA, Temel A (2004) Geochemical and Pb–Sr–Nd isotopic constraints indicating an enriched-mantle source for Late Cretaceous to Early Tertiary volcanism, central Anatolia, Turkey. Int Geol Rev 46:1022–1041

Alpaslan M, Boztug D, Frei R, Temel A, Kurt MA (2006) Geochemical and Pb–Sr–Nd isotopic composition of the ultrapotassic volcanics from the extension-related Çamardi-Ulukisla basin, Nigde province, central Anatolia, Turkey. J Asian Earth Sci 27:613–627

Appleby SK, Gillespie MR, Graham CM, Hinton RW, Oliver GJH, Kelly NM, EIMF (2010) Do S-type granites commonly sample infracrustal sources? New results from an integrated O, U–Pb and Hf isotope study of zircon. Contrib Mineral Petrol 160:115–132

Ataman G (1972) The preliminary study on the radiometric age of Cefalık Dagi that is one of the granitic-granodioiritic bodies in the SW of Ankara. J Hacettepe Fen ve Mühendislik Bilimleri 2:44–49 (in Turkish)

Aydar E, Gourdaud A, Deniel C, Lyberis N, Gündogdu N (1995) Quaternary volcanism of central Anatolia (Turkey)—association of calc-alkaline and alkaline magmatism in a zone of convergence. Can J Earth Sci 32:1058–1069

Aydin NS, Göncüoglu MC, Erler A (1998) Latest Cretaceous magmatism in the Central Anatolian Crystalline Complex: review of field, petrographic and geochemical features. Turk J Earth Sci 7:259–268

Belousova EA, Griffin WL, O'Reilly SY, Fisher NI (2002) Igneous zircon: trace element composition as an indicator of source rock type. Contrib Mineral Petrol 143:602–622

Bingöl E (1989) Geological map of Turkey, 1:2, 000, 000. Mineral Research and Exploration Institute, Ankara

Boztug D (1998) Post-collisional central Anatolian alkaline plutonism, Turkey. Turk J Earth Sci 7:145–165

Boztug D (2000) S-I-A-type intrusive associations: geodynamic of significance of synchronism between metamorphism and magmatism in central Anatolia, Turkey. In: Bozkurt E, Winchester JA, Piper JDA (eds) Tectonics and magmatism in Turkey and the surrounding area. Geol Soc Lond Spec Publ 173:441–458

Boztug D, Arehart GB (2007) Oxygen and sulfur isotope geochemistry revealing a significant crustal signature in the genesis of the post-collisional granitoids in central Anatolia, Turkey. J Asian Earth Sci 30:403–416

Boztug D, Harlavan Y (2008) K–Ar ages of granitoids unravel the stages of Neo-Tethyan convergence in the eastern Pontides and central Anatolia, Turkey. Int J Earth Sci 97:585–599

Boztug D, Arehart GB, Platevoet B, Harlavan Y, Bonin B (2007a) High-K, calc-alkaline I-type granitoids from the composite Yozgat batholith generated in a post-collisional setting following continent-oceanic island arc collision in central Anatolia, Turkey. Mineral Petrol 91:191–223

Boztug D, Harlavan Y, Arehart GB, Satir M, Avcı N (2007b) K–Ar age, whole-rock and isotope geochemistry of A-type granitoids in the Divrigi-Sivas region, eastern-central Anatolia, Turkey. Lithos 97:193–218

Boztug D, Tichomirowa M, Bombach K (2007c) ^{207}Pb–^{206}Pb single-zircon evaporation ages of some granitoid rocks reveal continent-oceanic island arc collision during the Cretaceous geodynamic evolution of the central Anatolian crust, Turkey. J Asian Earth Sci 31:71–86

Boztug D, Temiz H, Jonckheere R, Ratschbacher L (2008) Punctuated exhumation and foreland basin formation and infilling in (circum)—Central Anatolia (Turkey) associated with the Neo-Tethyan closure. Turk J Earth Sci 17:673–684

Boztug D, Jonckheere RC, Heizler M, Ratschbacher L, Harlavan Y, Tichomirova M (2009) Timing of post-obduction granitoids from intrusion through cooling to exhumation in central Anatolia, Turkey. Tectonophysics 473:223–233. doi:10.1016/j.tecto.2008.05.035

Chu M-F, Chung S-L, Song B, Liu D, O'Reilly SY, Pearson NJ, Ji J, Wen D-J (2006) Zircon U–Pb and Hf isotope constraints on the Mesozoic tectonics and crustal evolution of southern Tibet. Geology 34:745–748. doi:10.1130/G22725.1

Didier J, Barbarin B (1991) Enclaves and granite petrology. Elsevier, Amsterdam, p 625

Düzgören-Aydin NS, Malpas J, Göncüoglu MC, Erler A (2001) A review of the nature of magmatism in central Anatolia during the Mesozoic post-collisional period. Int Geol Rev 43:695–710

Erler A, Göncüoglu MC (1996) Geologic and tectonic setting of the Yozgat batholith, northern Central Anatolian Crystalline Complex, Turkey. Int Geol Rev 38:714–726

Floyd PA, Yaliniz MK, Göncüoglu MC (1998) Geochemistry and petrogenesis of intrusive and extrusive ophiolitic plagiogranites, Central Anatolian Crystalline Complex, Turkey. Lithos 42:225–241

Floyd PA, Göncüoglu MC, Winchester JA, Yaliniz MK (2000) Geochemical character and tectonic environment of Neotethyan ophiolitic fragments and metabasites in the Central Anatolian Crystalline Complex, Turkey. In: Bozkurt E, Winchester JA, Piper JDA (eds) Tectonics and magmatism in Turkey and the surrounding area. Geol Soc Lond Spec Publ 173:183–202

Frei D, Gerdes A (2009) Precise and accurate in situ U–Pb dating of zircon with high sample throughput by automated LA-SF-ICP-MS. Chem Geol 261:261–270. doi:10.1016/j.chemgeo.2008.07.025

Gautier P, Bozkurt E, Bosse V, Hallot E, Dirik K (2008) Coeval extensional shearing and lateral underflow during Late Cretaceous core complex development in the Nigde Massif, Central Anatolia, Turkey. Tectonics 27:TC1003. doi:10.1029/2006TC002089

Gerdes A, Zeh A (2006) Combined U–Pb and Hf isotope LA-(MC)-ICP-MS analyses of detrital zircons: comparison with SHRIMP and new constraints for the provenance and age of an Armorican metasediment in central Germany. Earth Planet Sci Lett 249:47–61

Gerdes A, Zeh A (2009) Zircon formation versus zircon alteration—New insights from combined U–Pb and Lu–Hf in situ LA-ICP-MS analyses, and consequences for the interpretation of Archean zircon from the Central Zone of the Limpopo Belt. Chem Geol 261:230–243. doi:10.1016/j.chemgeo.2008.03.005

Göncüoglu MC (1986) Geochronological data from the southern part (Nigde area) of the Central Anatolian Massif. Bull Miner Res Explor Inst Turk 105(106):83–96

Göncüoglu MC (2009) Comment on "^{207}Pb–^{206}Pb single-zircon evaporation ages of some granitoid rocks reveal continent-oceanic island arc collision during the Cretaceous geodynamic evolution of the central Anatolian crust, Turkey"—Boztug, D., Tichomirowa, M. & Bombach, K., 2007, JAES 31, 71–86, J Asian Earth Sci 34:796–797. doi:10.1016/j.jseaes.2008.11.001

Göncüoglu MC (2010) Introduction to the geology of Turkey: geodynamic evolution of the pre-alpine and alpine terranes. MTA Monogr Ser, p 66. ISBN 978-605-4075-74

Göncüoglu MC, Türeli TK (1994) Alpine collision-type granitoids in the western Central Anatolian Crystalline Complex. J Kocaeli Univ 1:39–46

Göncüoglu MC, Toprak GMV, Kusçu I, Erler A, Olgun E (1991) Geology of the western part of the Central Anatolian Massif: part I southern part. Unpubl. Report No: 2909, Turkish Petroleum Company (in Turkish)

Göncüoglu MC, Dirik K, Kozlu H (1997) General characteristics of pre-Alpine and Alpine Terranes in Turkey: explanatory notes to the terrane map of Turkey. Annales Geologique de Pays Hellenique 37:515–536

Göncüoglu MC, Çapkinoglu S, Gürsu S, Noble P, Turhan N, Tekin UK, Okuyucu C, Göncüoglu Y (2007) The Mississippian in the central and eastern Taurides (Turkey): constraints on the tectonic setting of the Tauride-Anatolide Platform. Geol Carpatica 58:427–442

Görür N, Oktay FY, Seymen I, Sengör AMC (1984) Paleotectonic evolution of Tuzgölü basin complex, central Turkey. In: Dixon JE, Robertson AHF (eds) The geological evolution of the Eastern Mediterranean. Geol Soc Lond Spec Publ 17:81–96

Görür N, Tüysüz O, Sengör AMC (1998) Tectonic evolution of the central Anatolian basins. Int Geol Rev 40:831–850

Griffin WL, Pearson NJ, Belousova E, Jackson SE, O'Reilly SY, van Achterberg E, Shee SR (2000) The Hf isotope composition of cratonic mantle: LAM-MC-ICPMS analysis of zircon megacrysts in kimberlites. Geochim Cosmochim Acta 64:133–147

Griffin WL, Wang X, Jackson SE, Pearson NJ, O'Reilly SY, Xu X, Zhou X (2002) Zircon chemistry and magma mixing, SE China:

in situ analysis of Hf isotopes, Tonglu and Pingtan igneous complexes. Lithos 61:237–269
Güleç N (1994) Rb–Sr isotope data from the Agaçören granitoid (east of Tuz Gölü): geochronological and genetical implications. Turk J Earth Sci 3:39–43
Güleç N, Kadioglu YK (1998) Relative involvement of mantle and crustal components in the Agaçören granitoid (central Anatolia-Turkey): estimates from trace element and Sr-isotope data. Chemie der Erde-Geochemistry 58:23–37
Hanchar JM, Miller CF (1993) Zircon zonation patterns as revealed by cathodoluminescence and back-scattered electron images: implications for interpretation of complex crustal histories. Chem Geol 110:1–13
Harley SL, Kelly NM (2007) Zircon, tiny but timely. Elements 3:13–18
Harris N (1996) Radiogenic isotopes and interpretation of granitic rocks. Episodes 19:107–113
Hawkesworth CJ, Kemp AIS (2006a) Using hafnium and oxygen isotopes in zircons to unravel the record of crustal evolution. Chem Geol 226:144–162
Hawkesworth CJ, Kemp AIS (2006b) Evolution of the continental crust. Nature 443:811–817
Hoskin PWO, Kinny PD, Wyborn D, Chappell BW (2000) Identifying accessory mineral saturation during differentiation in granitoid magmas: an integrated approach. J Petrol 41:1365–1396
Ilbeyli N (2005) Mineralogical–geochemical constraints on intrusives in central Anatolia, Turkey: tectono-magmatic evolution and characteristics of mantle source. Geol Mag 142:187–207. doi:10.1017/S0016756805000476
Ilbeyli N (2008) Geochemical comparison of ultramafic-mafic cumulate rocks from the central Anatolian ophiolites. Int Geol Rev 50:810–825
Ilbeyli N, Pearce JA, Thirlwall MF, Mitchell JG (2004) Petrogenesis of collision-related plutonics in central Anatolia, Turkey. Lithos 72:163–182
Isik V, Lo C-H, Göncüoglu MC, Demirel S (2008) ^{39}Ar–^{40}Ar ages from the Yozgat batholith: preliminary data on the timing of Late Cretaceous extension in the Central Anatolian Crystalline Complex, Turkey. J Geol 116:510–526
Jackson SE, Pearson NJ, Griffin WL, Belousova EA (2004) The application of laser ablation-inductively coupled plasma-mass spectrometry to in situ U–Pb zircon geochronology. Chem Geol 211:47–69
Kadioglu YK (1996) Geology, petrography and geochemistry of Agaçören (Aksaray) magmatic rocks. Unpubl. Ph.D. thesis. Dept of Geological Engineering, Middle East Technical University, p 242
Kadioglu YK, Güleç N (1996) Mafic microgranular enclaves and interaction between felsic and mafic magmas in the Agaçören intrusive suite: evidence from petrographic features and mineral chemistry. Int Geol Rev 38:854–867
Kadioglu YK, Güleç N (1999) Types and genesis of the enclaves in central Anatolian granitoids. Geol J 34:243–256
Kadioglu YK, Dilek Y, Güleç N, Foland KA (2003) Tectonomagmatic evolution of bimodal plutons in the Central Anatolian Crystalline Complex, Turkey. J Geol 111:671–690
Kadioglu YK, Dilek Y, Foland KA (2006) Slab break-off and syncollisional origin of the Late Cretaceous magmatism in the Central Anatolian Crystalline Complex, Turkey. In: Dilek Y, Pavlides S (eds) Postcollisional tectonics and magmatism in the Mediterranean region and Asia. Geol Soc Am Spec Paper 409:381–415
Kemp AIS, Hawkesworth CJ, Paterson BA, Kinny PD (2006) Episodic growth of the Gondwana supercontinent from hafnium and oxygen isotopes in zircon. Nature 439:580–583
Kemp AIS, Hawkesworth CJ, Foster GL, Paterson BA, Woodhead JD, Hergt JM, Gray CM, Whitehouse MJ (2007) Magmatic and crustal differentiationhistory of granitic rocks from Hf–O isotopes in zircon. Science 315:980–983. doi:10.1126/science.1136154
Koçak K, Isik F, Arslan M, Zedef V (2005) Petrological and source region characteristics of ophiolitic hornblende gabbros from the Aksaray and Kayseri regions, central Anatolian crystalline complex, Turkey. J Asian Earth Sci 25:883–891
Köksal S, Göncüoglu MC (2008) Sr and Nd isotopic characteristics of some S-, I- and A-type granitoids from Central Anatolia. Turk J Earth Sci 17:111–127
Köksal S, Göncüoglu MC, Floyd PA (2001) Extrusive members of postcollisional A-Type magmatism in central Anatolia: Karahidir volcanics, Idisdagi-Avanos area, Turkey. Int Geol Rev 43:683–694
Köksal S, Romer RL, Göncüoglu MC, Toksoy-Köksal F (2004) Timing of post-collisional H-type to A-type granitic magmatism: U–Pb titanite ages from Alpine central Anatolian Granitoids (Turkey). Int J Earth Sci 93:974–989
Köksal S, Möller A, Frei D, Göncüoglu MC, Toksoy-Köksal F (2007) Petrological characteristics and LA-SF-ICP-MS U–Pb ages of S-type granitoids from central Turkey. Geochim Cosmochim Acta 71, Supplement 1, Goldschmidt Conference Abstracts A505
Köksal S, Göncüoglu MC, Toksoy-Köksal F, Möller A, Kemnitz H (2008) Zircon typologies and internal structures as petrogenetic indicators in contrasting granitoid types from central Anatolia. Mineral Petrol 93:185–211
Košler J, Fonneland H, Sylvester P, Tubrett M, Pedersen R-B (2002) U–Pb dating of detrital zircons for sediment provenance studies—a comparison of laser ablation ICPMS and SIMS techniques. Chem Geol 182:605–618
Kurt MA, Alpaslan M, Göncüoglu MC, Temel A (2008) Geochemistry of late stage medium to high-K calc-alkaline and shoshonitic dykes in the Ulukisla Basin (Central Anatolia, Turkey): petrogenesis and tectonic setting. Int Geochem 46:1143–1163
Millonig L, Zeh A, Gerdes A, Klemd R, Barton JM (2010) Decompressional heating of the Mahalapye complex (Limpopo belt, Botswana): a response to Palaeoproterozoic magmatic underplating? J Petrol 51:703–729. doi:10.1093/petrology/egp097
Nasdala L, Hofmeister W, Norberg N, Mattinson JM, Corfu F, Dörr W, Kamo SL, Kennedy AK, Kronz A, Reiners PW, Frei D, Košler J, Wan Y, Götze J, Häger T, Kröner A, Valley JW (2008) Zircon M257—a homogeneous natural reference material for the ion microprobe U–Pb analysis of zircon. Geostand Geoanal Res 32:247–265
Paterson BA, Stephens WE, Rogers G, Williams IS, Hinton RW, Herd DA (1992) The nature of zircon inheritance in two granite plutons. Trans R Soc Edinb Earth Sci 83:459–471
Pupin JP (1980) Zircon and granite petrology. Contrib Mineral Petrol 73:207–220
Qin J-F, Lai S-C, Diwu C-R, Ju Y-J, Li Y-F (2010) Magma mixing origin for the post-collisional adakitic monzogranite of the Triassic Yangba pluton, Northwestern margin of the South China block: geochemistry, Sr–Nd isotopic, zircon U–Pb dating and Hf isotopic evidences. Contrib Mineral Petrol 159:389–409. doi:10.1007/s00410-009-0433-2
Scherer E, Münker C, Mezger K (2001) Calibration of the lutetium-hafnium clock. Science 293:683–687
Scherer E, Whitehouse MJ, Münker C (2007) Zircon as a monitor of crustal growth. Elements 3:19–24
Schermaier A, Haunschmid B, Schubert G, Frasl G, Finger F (1992) Diskriminierung von S-Typ und I-Typ Graniten auf der Basis

zirkontypologischer Untersuchungen. Frankfurter Geowissenschaftliche Arbeiten Serie A Geologie-Paläontologie 11:149–153

Sengör AMC, Yilmaz Y (1981) Tethyan evolution of Turkey: a plate tectonic approach. Tectonophysics 75:181–241

Siebel W, Chen F (2010) Zircon Hf isotope perspective on the origin of granitic rocks from eastern Bavaria, SW Bohemian massif. Int J Earth Sci 99:993–1005. doi:10.1007/s00531-009-0442-4

Sláma J, Košler J, Condon DJ, Crowley JL, Gerdes A, Hanchar JM, Horstwood MSA, Morris GA, Nasdala L, Norberg N, Schaltegger U, Schoene B, Tubrett MN, Whitehouse MJ (2008) Plešovice zircon—a new natural reference material for U–Pb and Hf isotopic microanalysis. Chem Geol 249:1–35

Stampfli GM, Borel GD (2002) A plate tectonic model for the Paleozoic and Mesozoic constrained by dynamic plate boundaries and restored synthetic oceanic isochrons. Earth Planet Sci Lett 196:17–33

Sun S-S, McDonough WF (1989) Chemical and isotopic systematics of oceanic basalts; implications for mantle composition and processes. In: Saunders AD, Norry MJ (eds) Magmatism in the ocean basins. Geol Soc Lond Spec Publ 42:313–345

Toksoy-Köksal F, Göncüoglu MC, Yalınız MK (2001) Petrology of the Kurancali phlogopite metagabbro: an island arc-type ophiolitic sliver in the Central Anatolian Crystalline Complex. Int Geol Rev 43:624–639

Vavra G (1990) On the kinematics of zircon growth and its petrogenetic significance: a cathodoluminescence study. Contrib Mineral Petrol 106:90–99

Vavra G (1994) Systematics of internal zircon morphology in major Variscan granitoid types. Contrib Mineral Petrol 117:331–344

Voshage H, Hofmann AW, Mazzucchelli M, Rivalenti G, Sinigoi S, Raczek I, Demarchi G (1990) Isotopic evidence from the Ivrea zone for a hybrid lower crust formed by magmatic underplating. Nature 347:731–736

Whitehouse MJ, Kemp AIS (2010) On the difficulty of assigning crustal residence, magmatic protolith and metamorphic ages to Lewisian granulites: constraints from combined in situ U–Pb and Lu–Hf isotopes. In: Law RD, Butler RWH, Holdsworth RE, Krabbendam M, Strachan RA (eds) Continental tectonics and mountain building: the legacy of peach and horne. Geol Soc Lond Spec Publ 335:81–101. doi:10.1144/SP335.5

Whitney DL, Dilek Y (1997) Core complex development in central Anatolia. Geology 25:1023–1026

Whitney DL, Teyssier C, Fayon AK, Hamilton MA, Heizler M (2003) Tectonic controls on metamorphism, partial melting, and intrusion: timing and duration of regional metamorphism and magmatism in the Nigde Massif, Turkey. Tectonophysics 376:37–60

Yaliniz MK, Floyd PA, Göncüoglu MC (1996) Supra-subduction zone ophiolites of central Anatolia, geochemical evidence from the Sarikaraman ophiolite, Aksaray, Turkey. Mineral Mag 60:697–710

Yaliniz MK, Aydin NS, Göncüoglu MC, Parlak O (1999) Terlemez quartz monzonite of central Anatolia (Aksaray-Sarikaraman): age, petrogenesis and geotectonic implications for ophiolite emplacement. Geol J 34:233–242

Yaliniz MK, Floyd PA, Göncüoglu MC (2000) Geochemistry of volcanic rocks from the Çiçekdag ophiolite, central Anatolia, Turkey, and their inferred tectonic setting within the northern branch of the Neotethyan ocean. In: Bozkurt E, Winchester JA, Piper JDA (eds) Tectonics and magmatism in Turkey and the surrounding area. Geol Soc Lond Spec Publ 173:203–218

Yang J-H, Wu F-Y, Chung S-L, Wilde SA, Chu M-F (2006) A hybrid origin for the Qianshan A-type granite, northeast China: geochemical and Sr–Nd–Hf isotopic evidence. Lithos 89:89–106

Yilmaz S, Boztug D (1998) Petrogenesis of the Çiçekdag Igneous Complex, N of Kirsehir, central Anatolia, Turkey. Turk J Earth Sci 7:185–199

Zeh A, Gerdes A, Klemd R, Barton JM (2007) Archaean to Proterozoic crustal evolution in the central zone of the Limpopo belt (south Africa-Botswana): constraints from combined U–Pb and Lu–Hf isotope analyses of zircon. J Petrol 48:1605–1639

Zheng YF, Zhang SB, Zhao ZF, Wu YB, Li XH, Li ZX, Wu FY (2007) Contrasting zircon Hf and O isotopes in the two episodes of Neoproterozoic granitoids in South China: implications for growth and reworking of continental crust. Lithos 96:127–150

Zhong H, Zhu W-G, Hu R-Z, Xie LW, He D-F, Liu F, Chu Z-Y (2009) Zircon U–Pb age and Sr–Nd–Hf isotope geochemistry of the Panzhihua A-type syenitic intrusion in the Emeishan large igneous province, southwest China and implications for growth of juvenile crust. Lithos 110:109–128